AN OBJECTIVE ANALYSIS OF THE PROPAGATING CIRCULATION FEATURES ASSOCIATED WITH MIDWEST PRECIPITATION VARIABILITY

by

Jessica M. Liptak

A thesis submitted to the faculty of
The University of Utah
in partial fulfillment of the requirements for the degree of

Master of Science

Department of Atmospheric Sciences

The University of Utah

August 2011

The University of Utah Graduate School

STATEMENT OF THESIS APPROVAL

The thesis of **Jessica M. Liptak**

has been approved by the following supervisory committee members:

Courtenay Strong	, Chair	**5/13/2011** Date Approved
John Horel	, Member	**5/13/2011** Date Approved
Thomas Reichler	, Member	**5/13/2011** Date Approved

and by **Jim Steenburgh** , Chair of

the Department of **Atmospheric Sciences**

and by Charles A. Wight, Dean of the Graduate School.

ABSTRACT

The main objectives of this study were to identify the leading propagating patterns of atmospheric variability over the Midwest, and to determine the relationships of these patterns with Midwest precipitation. Complex Hilbert empirical orthogonal function (HEOF) analysis was performed on daily mean 850-hPa horizontal moisture transport, 850-hPa temperature advection, jet relative frequency, and the difference between 850-hPa and 250-hPa vorticity advection. Atmospheric fields were derived from the 6-hourly NCEP-NCAR reanalysis on a year-round and within-season basis. Additionally, the HEOFs were phase-shifted to maximize the correlation between the real part of the score series and area-weighted power-transformed Midwest precipitation.

In the year-round analysis, the leading HEOF of combined jet relative relative frequency and 850-hPa horizontal moisture transport captured the seasonal migration of the jet and attendant low-level circulation features. The second HEOF showed high jet relative frequency over the Midwest on the upstream side of a trough, and moisture transport from the Gulf of Mexico into the Midwest. The leading within-season HEOF of combined jet relative relative frequency and 850-hPa horizontal moisture transport showed a similar pattern in winter, spring, and fall. In all seasons, the monthly mean scores of the leading HEOF of combined jet relative relative frequency and 850-hPa horizontal moisture transport were better estimates of Midwest precipitation than the Pacific-North American pattern, North Atlantic Oscillation,

and El Niño-Southern Oscillation teleconnection indices.

In addition, this study examined the relationship between the leading winter propagating patterns of variability and lake effect precipitation over the Great Lakes region. Here, the leading HEOF of combined jet relative relative frequency and 850-hPa horizontal moisture transport was phase-shifted to maximize the correlation between the real part and a lake effect precipitation fraction time series. The phase-shifted HEOF did not resolve the mesoscale features of lake effect snow, but did position the synoptic-scale circulation so that flow developed the expected northerly component over the Great Lakes.

TABLE OF CONTENTS

LIST OF FIGURES

LIST OF TABLES

CHAPTER 1

INTRODUCTION

1.1 Global precipitation trends

Much of the literature regarding precipitation has focused on data averaged over large areas that span the past 50 to 100 years. Trenberth et al. (2007) showed that trends in global average precipitation anomalies derived from the 1900–2005 Global Historical Climate Network (GHCN; Vose et al., 1992) and 1901–2002 CRU TS 2.1 (Mitchell and Jones, 2005) datasets were statistically insignificant owing to the cancellation effects of regional precipitation anomalies. For example, annual precipitation trends were positive over most of North America and Australia, but largely negative over western Africa and South America. Furthermore, these trends were sensitive to the time period used. During 1970–2005, annual precipitation increased over much of western Africa, while most of North America showed almost no trend, except for the southwest United States (U.S.) where precipitation decreased.

In addition, trends in precipitation totals may be misleading, since they do not tell whether increases or decreases result from changes in precipitation intensity (individual events generating more or less precipitation than normal), frequency (more or fewer overall events in a given interval), or a combination of the two. In fact, trends in frequency and/or intensity may be present without a significant trend in mean precipitation. Karl and Knight (1998)

addressed this issue by expressing the trend in total precipitation as the sum of the trends in event frequency and intensity, and assessing both components for different precipitation percentiles over eight subregions in the conterminous U.S. The study found that increases in both the intensity and frequency of events over all subregions contributed to the upward trend in annual precipitation over the conterminous U.S. Annual increases in intensity over most of the subregions primarily resulted from increases in "heavy" (90^{th} to 95^{th} percentile) and "extreme" ($> 95^{th}$ percentile) events. These findings agree with those of Groisman et al. (2004) and Groisman et al. (2005), which showed statistically significant increases in days with "very heavy" ($> 99.7^{th}$ percentile) precipitation for parts of the central U.S., with all of the increase taking place after approximately 1970.

The incidence of extreme precipitation events has also been measured in terms of return periods, or recurrence intervals. From 1931 to 1996, the frequency of 7-day events with one-year return periods increased over a broad area extending from the Southwest northeast into the north-central U.S., though only the trend over the northern Great Lakes region was significant (Kunkel et al., 1999). Trends are similar for combinations of 1- and 20-year return periods and 1-, 5-, and 30-day intervals (Kunkel, 2003). By approximating precipitation with Generalized Extreme Value (GEV) distributions, DeGaetano (2009) found increases in the precipitation amounts corresponding to 2-, 50-, and 100-year return periods (or, alternately, decreases in the median return periods for certain precipitation amounts) over most of the U.S., especially in the Northeast and western Great Lakes region. This was the case for both partial-duration series (time series of varying lengths) and 30-year running series spanning 1950 to 2007, where changes were computed with respect to 1950–1979 return period values.

1.2 Regional precipitation and cyclone trends

Given the variability in precipitation trends and behavior, regional studies provide a useful perspective. In addition to circumventing trend cancellation, regional analysis results may have greater value in terms of practical application; engineers do not design structures to withstand global mean values of rainfall, nor do farmers plant crops based on the annual average precipitation over the conterminous U.S. Owing to the varying quality and extent of data sets among regions, some locations are better suited for long-term precipitation analysis than others. As such, this research focuses on changes in the Midwest U.S., as it has a relatively dense precipitation network with most station data extending to at least the 1950s. The Midwest also has the advantages of a lack of direct influence by tropical systems and high terrain, making it easier detect relationships between precipitation and possible synoptic scale driving mechanisms.

Taking into consideration the spatial scale of precipitation systems, Konrad (2001) found that extreme precipitation computed from maximum mean 2-day precipitation totals increased for small (2500 km^2), medium (100,000 km^2), and large (500,000 km^2) events over the Midwest (displaced somewhat west of the domain used in this study) from 1950 to 1996. Konrad (2001) also examined the seasonal distribution of the centroids of events in the three size categories, and found that most large-scale events were concentrated in late spring (MAM) and early summer (JJA), while about 60% of small-scale events occurred in July and August.

Shifts in precipitation may also be tied to trends in occurrence or characteristics of cyclones and storm tracks. The Midwest is collocated with a maximum in cyclone frequency centered over the Great Lakes (e.g., Zishka and Smith, 1980; Reitan, 1974; Wernli and

Schwierz, 2006). In winter, this area is part of two cyclone trajectories that extend from Colorado and Alberta in the lee of the Rocky Mountains, while summer cyclones originate near eastern Montana and tend to follow a path along the U.S.-Canada border (Zishka and Smith, 1980; Isard et al., 2000). In addition, strong cyclones, defined as those with a central pressure $\leq$ 992 mb, increased over the Great Lakes region on an annual basis from 1900 to 1990 (Angel and Isard, 1998). This increase was concentrated in the November–April cold season, and occurred during 1900–1950 and 1985–1990. The frequency of *all* Great Lakes cyclones, however, decreased prior to 1939, and exhibited no significant trend between 1966 and 1990. These results differ from those for the U.S. as a whole, in which 1905–1940 was characterized by an increase in cyclone totals, followed by a decrease between approximately 1950 and 1985 (Reitan, 1979), then another increase through the mid-1990s (Agee, 1991; Chagnon, 1995). Conversely, Hayden (1999) found no change in the frequency or intensity of storm tracks over North America during 1885–1996.

Angel and Isard (1998) showed that monthly average precipitation had significant positive correlations with the frequency of strong cyclones during most of the cold season, as well as September and August, over the 90-year period. Konrad (2001) also noted that late-spring large- and medium-scale precipitation events were often associated with 500-hPa cyclones, and that the upward trends in both categories paralleled the increase in North American cyclone frequencies found in Key and Chan (1999). Similarly, Trigo and Davies (2000) found decreases in 1979–1996 October–March northern Mediterranean precipitation were associated with a reduced occurrence of intense cyclones.

In the northeast U.S., Bradbury et al. (2003) found that winter precipitation was related to the first two rotated principal components (RPCs) of cyclone frequency, both of

which emphasized the influence of marine cyclones that commonly track along the East Coast. However, neither of these RPCs exhibited significant trends; rather, the first RPC was characterized by low-frequency variability associated with the Southern Oscillation Index (SOI) and the Pacific Decadal Oscillation (PDO), while the second was related to regional sea surface temperature (SST) patterns. Results from Hartley and Keables (1998) revealed a similar East Coast cyclone track in composites of cyclonic activity for the seven highest scores from the leading (unrotated) PC of New England winter snowfall. Though decadal variability in the PC time series was related to regional SSTs as in Bradbury et al. (2003), snowfall was not significantly related to the SOI. Furthermore, cyclonic activity was enhanced over interior New England for high-score cases of general precipitation and low-score cases of snowfall. The increased likelihood of snowfall associated with coastal cyclones was attributed to the tendency of these systems to produce more low-level cold advection into the area.

1.3 Regional influence of teleconnections

Teleconnections impact precipitation and its associated processes in the Midwest, particularly during winter months. Angel and Isard (1998) found that the Pacific-North American (PNA) pattern was anticorrelated with strong cyclone occurrence over the Great Lakes during November, December, and January. Likewise, an inverse relationship between precipitation in winter months and the PNA index was documented over the Ohio River Valley (ORV) (Coleman and Rogers, 2003) and the Midwest in general (Leathers et al., 1991; Serreze et al., 1998). In addition, Isard et al. (2000) found that Great Lakes cyclones occurred more frequently over Canada during the positive phase of the PNA, and over the southwest U.S.

in the lee of the Rockies during the negative phase.

Precipitation is also influenced by the El Niño–Southern Oscillation (ENSO), where El Niño events, characterized by warm SST anomalies in the eastern equatorial Pacific, are associated with reduced precipitation over the Midwest, primarily in the vicinity of the ORV during winter (e.g., Gershunov and Barnett, 1998a; Mo and Schemm, 2008; Becker and Berbery, 2009; Zhang et al., 2010). Eichler and Higgins (2006) showed corresponding changes in winter storm tracks, with the Midwest experiencing an increase in surface cyclone frequency during La Niña events. However, the results of Becker and Berbery (2009) revealed a relative increase in the intensity of winter daily precipitation (1975–2005) over the upper Midwest during El Niño events, and a decrease in intensity over the ORV (their Fig. 9).

The precipitation anomalies associated with ENSO in other seasons differ from those in winter. While composites of SST anomalies in a study by Bates and Hoerling (2001) depicted warm anomalies in the east Pacific during the 10 wettest spring (April–June) periods in the central U.S., the overall correlation between central U.S. precipitation and Pacific SST anomalies was not significant. Furthermore, no corresponding SST pattern was present in the composite analysis for the driest springs. For summer, Higgins et al. (2007) showed that portions of the upper Midwest experienced 5–10 % more days with precipitation > 1 mm, as well as greater accumulated heavy ($>$ 90th percentile) precipitation, in JAS during moderate–strong El Niño events compared to La Niña events (their Figs. 6 and 7, respectively). Composite El Niño–La Niña difference maps in Mo and Schemm (2008) (their Fig. 9) revealed similar patterns in daily precipitation anomalies during JAS and, to a lesser extent, ASO.

Decadal variability of Midwest precipitation is largely governed by the Pacific Decadal Oscillation (PDO; Mantua et al., 1997), which is linked to ENSO (e.g., Gershunov and Barnett, 1998b; Newman et al., 2003; Schneider and Cornuelle, 2005). The positive phase of the PDO is defined by positive SST anomalies that extend from the Gulf of Alaska, along the West Coast into the central equatorial Pacific (Mantua et al., 1997). This "warm horse shoe" surrounds an area of cold SST anomalies in the central Pacific. From the 1950s through the mid 1970s, the PDO tended toward a negative phase, followed by a predominantly positive phase in subsequent decades (e.g., Mauget, 2003; Schneider and Cornuelle, 2005). In general, a positive PDO phase corresponds to an increase in summer precipitation over portions of the Midwest (Barlow et al., 2001; Higgins et al., 2007). Higgins et al. (2007) also showed that the PDO accounts for most of the contribution of the observed difference in precipitation in the central U.S. between the 1976–2004 and 1948–1975 periods, though the significant area only includes the southwest portion of the Midwest (their Fig. 11). However, Ault and George (2010) found that decadal variability only comprises a significant portion (i.e., $> 10\%$) of the variance in winter precipitation for a few locations in the U.S., including Minnesota.

To summarize, positive trends in extreme precipitation frequency and intensity have occurred over the Midwest during the past 50 to 100 years. However, most studies tend to consider changes in precipitation separately from potential driving mechanisms, such as shifts in cyclone occurrence, both of which are tied to ENSO and other patterns of low-frequency variability. Overall, much uncertainty exists regarding the relationship among precipitation, associated atmospheric features, and teleconnections in the Midwest. Furthermore, few studies have examined the relationship between propagating circulation patterns

and regional precipitation. Thus, the main objective of this study is to bridge this gap through detailed investigation of the propagating synoptic scale patterns of variability that link Midwest precipitation to larger-scale standing wave teleconnections.

CHAPTER 2

DATA AND METHODS

2.1 Data

2.1.1 Precipitation and atmospheric fields

The Midwest was defined as the area bounded by 36°–46°N and 83°–95°W – essentially the region encompassing the Upper Mississippi and Midwest subregions in Groisman et al. (2004) and Groisman et al. (2005). Daily (00:00–23:59 UTC) total precipitation in mm from 1 December 1957 to 28 February 2009 was obtained from the Global Historical Climate Network (GHCN) daily dataset available from the National Climatic Data Center (NCDC; http://www.ncdc.noaa.gov/). A total of 150 stations within the Midwest were retained after the inspection of all data, ensuring that no more than 10% of the measurements were missing from any record.

Atmospheric fields described in subsections 2.2.2–2.2.4 were based on daily values derived from the NCEP-NCAR Reanalysis (NNR) (Kalnay et al., 1996) provided by the Physical Sciences Division of the NOAA Earth Systems Research Laboratory (NOAA/OAR/ESRL PSD) in Boulder, CO (http://www.esrl.noaa.gov). Six-hourly values were developed for each field, and daily means were then calculated to match the daily mean precipitation data.

2.1.2 Teleconnections

Monthly mean values of two teleconnection indices were obtained from the Climate Prediction Center (http://www.cpc.ncep. noaa.gov): the North Atlantic Oscillation (NAO; Barnston and Livezey, 1987), and the PNA (Wallace and Gutzler, 1981). Both teleconnection indices were computed from the rotated principal components (e.g., Horel, 1981; Barnston and Livezey, 1987) of standardized 500-hPa height anomalies based on the three-month period centered on each month. The Multivariate ENSO Index (MEI; Wolter and Timlin, 1993, 1998) is defined based on the first unrotated principal component of combined sea level pressure, surface u and v winds, SST, surface air temperature, and cloud cover over the central Pacific from the Comprehensive Ocean-Atmosphere Data Set (COADS). Bimonthly MEI values were obtained from the NOAA/OAR/ESRL PSD (http://www.esrl. noaa.gov).

2.2 Derived variables

2.2.1 Area-weighted Midwest precipitation

Voronoi weighting was applied to the Midwest precipitation stations that were retained following the initial quality control procedures. The process of constructing Voronoi diagrams is detailed in Aurenhammer (1991). For a particular station *p*, a polygon was drawn around that station whose edges were closer to *p* than any other adjacent site. Fig. 1 shows the Voronoi map for the Midwest stations. The bounds for the Voronoi mapping scheme were extended beyond the Midwest to avoid errors in polygon construction that occur at the edges of the domain. The area within the polygon defined the weight *w* applied to the station. Thus, the area-weighted precipitation for the Midwest is given by

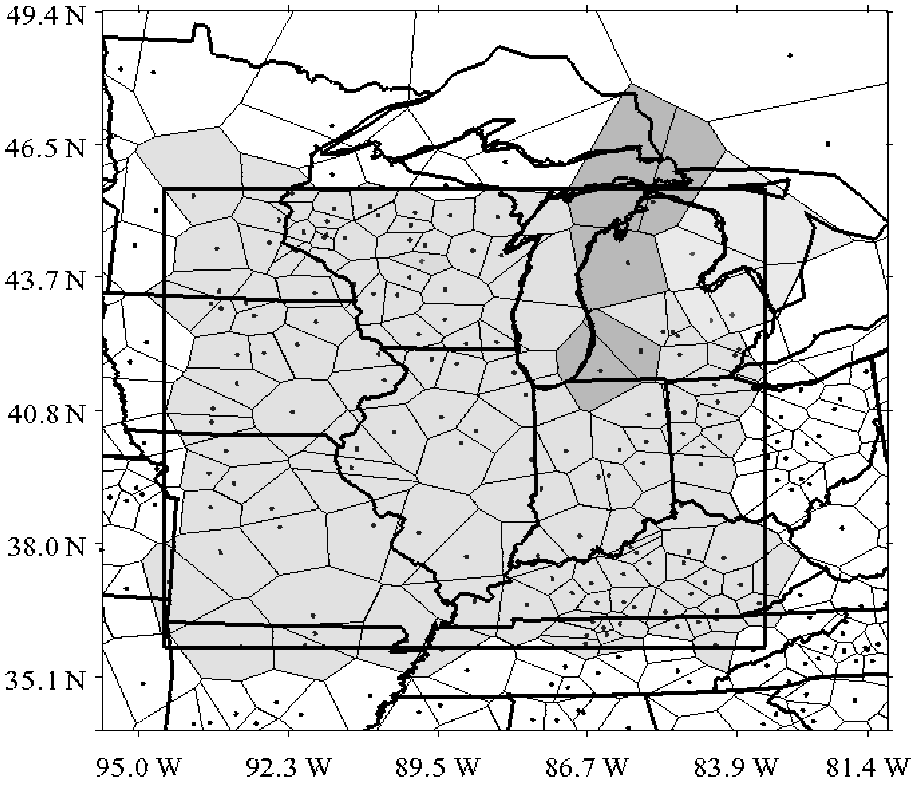

Fig. 1: The region within the black box defines the Midwest. Dots show the locations of precipitation stations, and thin lines indicate Voronoi polygons. Light gray shading indicates Voronoi polygons included in the Midwest domain, and dark gray shading denotes the Midwest polygons that were used to define the lake effect snow index in section 3.4.

$$P = \frac{\sum_{i=1}^{n} p_i w_i}{\sum_{i=1}^{n} w_i}\,, \tag{1}$$

where n is the number of stations in the domain. Shifting the Midwest latitude and longitude bounds by $\pm 2.5^\circ$ yielded precipitation time series correlated with P at $r \geq 0.95$, meaning that the results presented here are robust to realistically-sized changes in the definition of the Midwest.

Since the precipitation time series was positively skewed, a power transformation was applied to P (Fig. 2). The optimal power transformation was determined by minimizing the d statistic (Hinkley, 1977)

$$d = \frac{|\text{mean} - \text{median}|}{\text{spread}}\,, \tag{2}$$

and corresponded to raising precipitation to the power $1/4$. The transformed Midwest precipitation time series (Fig. 2c,d) more closely approximated a Gaussian distribution than the raw precipitation time series (Fig 2a,b). The trends in the raw and transformed precipitation time series are 1.5×10^{-5} mm day^{-1}(5.5×10^{-2} mm decade^{-1}) and 3.2×10^{-6} mm$^{0.25}$day^{-1} (1.2×10^{-2} mm$^{0.25}$ decade^{-1}). Because of the large sample size ($n = 18718$), these small trends are significant at $\alpha = 0.05$ under bootstrapping.

2.2.2 Temperature advection and vorticity advection

Temperature advection at 850 hPa, denoted *TA*, (K s^{-1}) and the difference in vorticity advection between 850 and 250 hPa, denoted *VA* (s^{-2}), were analyzed because they are

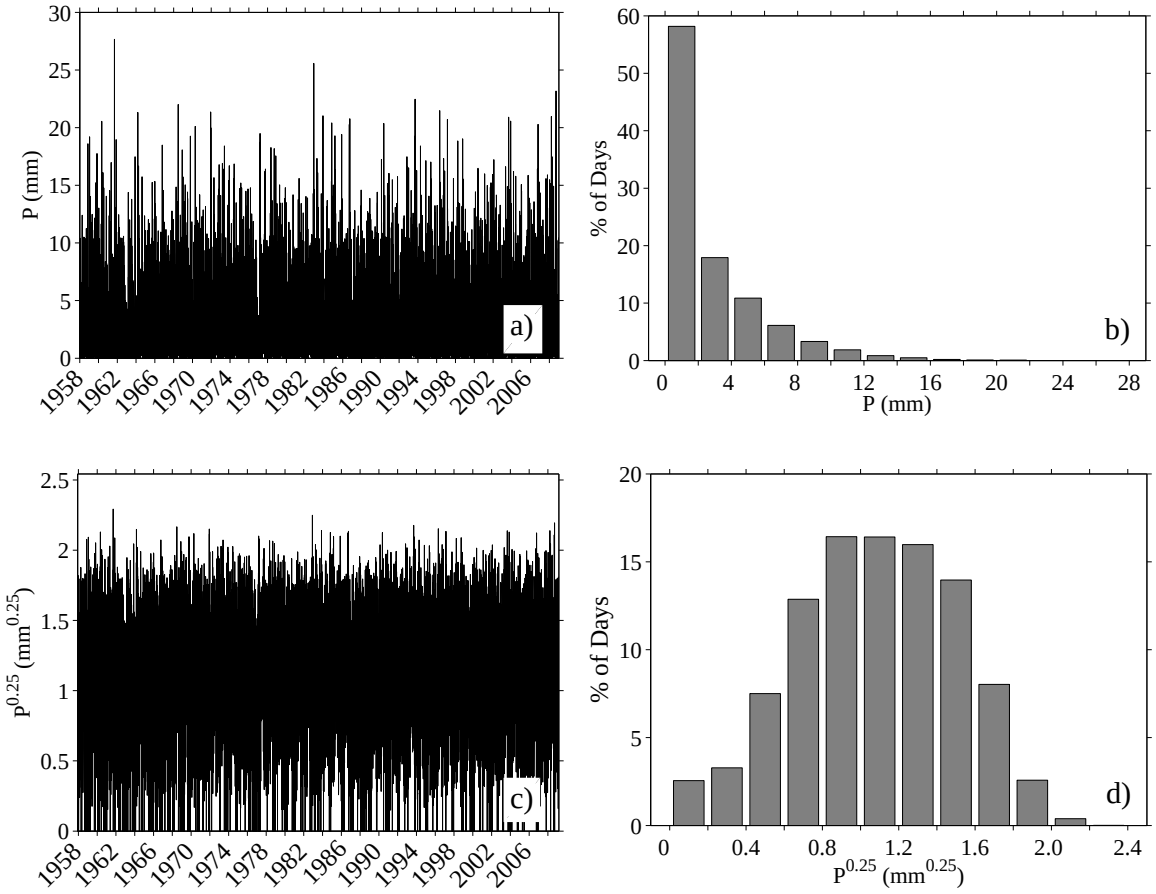

Fig. 2: Time series and histogram of P and $P^{0.25}$. a) and b) correspond to P. c) and d) correspond to $P^{0.25}$. In a) and c), years are indicated at 01 January.

closely related to geostrophic temperature and differential vorticity advection, which are associated with large-scale vertical motion according to the traditional omega equation (e.g., Holton, 2004).

Upward motion, indicated by negative values of omega, is conducive to the formation of clouds and precipitation in a sufficiently moist environment. Negative omega is diagnosed when low-level geostrophic temperature advection and differential vorticity advection are positive (i.e., geostrophic vorticity advection becomes more positive or less negative with decreasing pressure). However, the geostrophic assumption overestimates the observed wind in troughs and underestimates the observed wind in ridges. Thus, *VA* and *TA* were used instead of omega to approximate large-scale vertical motion.

2.2.3 Jet stream relative frequency

The relative frequency of jet stream occurrence in the upper troposphere, denoted $\tilde{C}$, was derived from the surface of maximum wind (SMW), which is defined as the surface passing through the greatest wind speed in each column from 500 hPa to the tropopause or the upper bound of tropospheric jet streams extending into the lower stratosphere (Strong and Davis, 2005). Use of the SMW rather than wind speed on a constant pressure surface takes into consideration horizontal variations in jet-core pressure. In the example in Fig. 3, filled circles denote the SMW at each latitude. Applying the method used in Strong and Davis (2008), $\tilde{C}$ was computed by dividing the number of times a jet occurred at a grid point by the total number of observations in a given time period.

The mean 1958–2008 $\tilde{C}$ pattern (Fig. 4) captures the seasonal shift in both the polar and subtropical jets. High $\tilde{C}$ over the eastern U.S. in winter (DJF) (Fig. 4a) indicates the

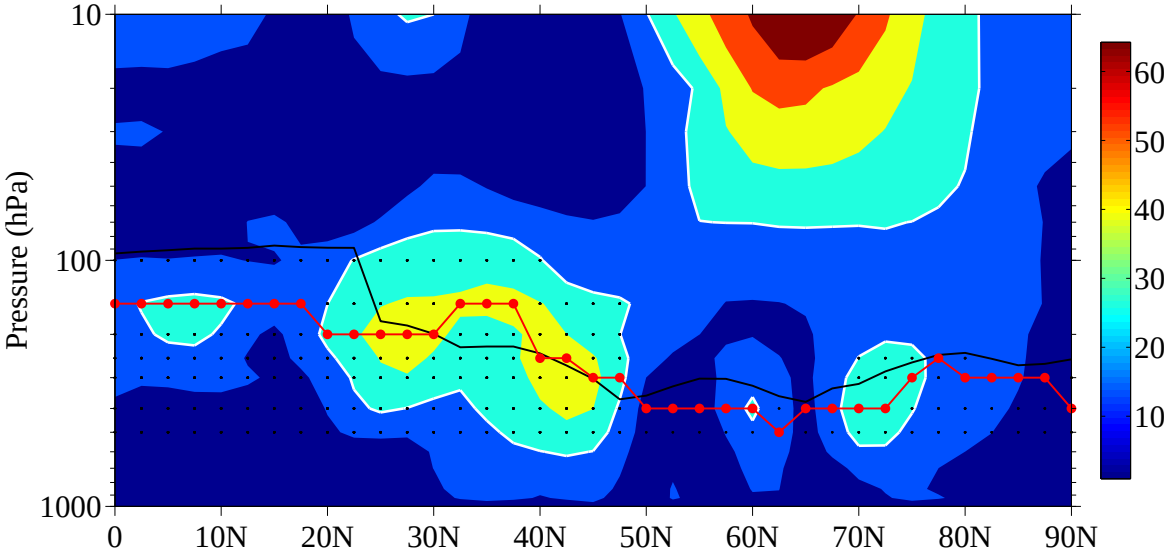

Fig. 3: Wind speed (m s^{-1}), tropopause pressure (hPa), and the SMW along 90°W. The solid black line indicates the tropopause. Black circles indicate candidates for SMW pressures, and filled red circles indicate the SMW. Areas containing speeds $\geq$ 25.7 m s^{-1} (50-knot) are outlined in white.

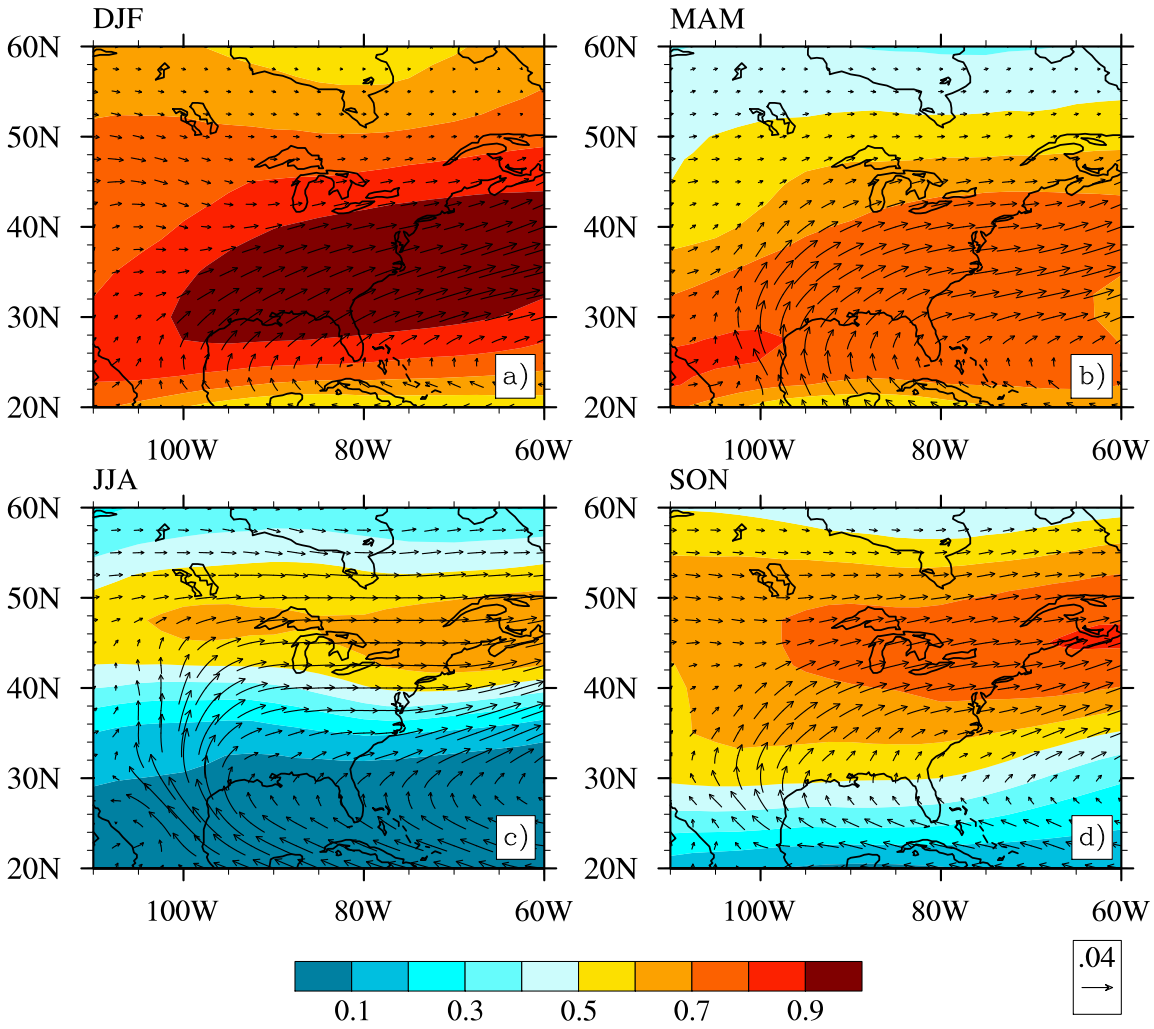

Fig. 4: 1958–2008 composite mean $\tilde{C}$ (filled contours) and $q\mathbf{v}$ (arrows) for a) DJF, b) MAM, c) JJA, and d) SON.

mean position of the eddy-driven jet, and a trough over the eastern U.S. reflects the frequent occurrence of synoptic waves. In spring (MAM) (Fig. 4c), $\tilde{C}$ values decrease over most of the contiguous U.S. as the eddy-driven jet migrates north, and the local maximum over Mexico indicates the subtropical jet. $\tilde{C}$ is maximized over Canada in summer (JJA) (Fig. 4c), and the seasonal minimum in synoptic wave activity is indicated by ridging over the central U.S. In fall (SON) (Fig. 4d), relatively high $\tilde{C}$ values over eastern U.S. signal the return of the eddy-driven jet. As in DJF, a mean trough over the eastern U.S. indicates an increase in the occurrence of synoptic waves.

2.2.4 Horizontal moisture transport

To analyze horizontal moisture transport, the vector field $q\mathbf{v} \equiv (qu, qv)$ was calculated at 850 hPa. $q\mathbf{v}$ yielded propagating patterns that were highly correlated with Midwest precipitation during all seasons (Section 3.3). The vector field proved to be more useful than the scalar moisture advection ($-\mathbf{v} \cdot \nabla q$) because $q\mathbf{v}$ indicates the magnitude and direction of moisture transport.

Though vertically integrated horizontal moisture flux is a more complete measure of atmospheric moisture transport, its use would have had a minimal impact on the correlation between precipitation and moisture transport, as most atmospheric water vapor is concentrated in the lower troposphere. Furthermore, the Great Plains Low-Level Jet (GPLLJ), an important means of moisture flow from the Gulf of Mexico to the central U.S., is often present at the 850-hPa level, though its peak wind speeds typically occur below it at approximately 750 to 1000 m above ground level (Bonner, 1968; Mitchell et al., 1995).

2.3 Statistical methods

2.3.1 Bootstrapping

Bootstrapping was used to test the statistical significance of all Pearson correlation coefficients (r) reported here. The process (e.g., Wilks, 1995; Horowitz, 2001) involves resampling the data to empirically determine the sampling distribution of r. Bootstrapping makes no assumptions about the shape of the distribution, and is thus suited for the precipitation data.

Bootstrapped samples were constructed by selecting n pairs of values with replacement from a sample of n pairs, and r was calculated for each bootstrapped sample. A total of 1000 bootstrapped samples were developed for each correlation, and the $\alpha = 0.05$ confidence interval of the bootstrapped distribution was determined using the percentile method, where the interval (100-α) was bounded by $(1-\alpha)/2$ and $\alpha/2$ (Efron, 1981). If the values that defined the 2.5^{th} and 97.5^{th} percentiles of the bootstrapped r distribution were of the same sign, there was a 5% chance that the correlation coefficient arose from sampling variability alone .

2.3.2 Empirical orthogonal function analysis

Empirical orthogonal function (EOF) analysis, or principal component analysis, has often been used in climate studies to objectively identify leading modes, or patterns, of atmospheric variability. Traditional EOF analysis has many variations, all of which are based on the process initially outlined in Lorenz (1956), which seeks to limit the size of a data set such that only the factors that explain the most variance in the data are retained. More specifically, the data are manipulated to create linear combinations of variables that are uncorrelated with one another, and explain a large fraction of the variance in the original

data set. Each linear combination is ordered so that the first combination explains the most variance in the data, the second combination explains the second largest amount of variance, and so on. The standard method of traditional EOF analysis is briefly outlined here to establish notation that will be used to define a phase shift for complex Hilbert EOFs in subsection 2.3.3.

Following the presentation in Jolliffe (2002) and Hannachi et al. (2007), EOF analysis is performed by arranging a field measured at $t = 1, \ldots, n$ times and $j = 1, \ldots, p$ locations as the $n \times p$ centered (zero time-mean) matrix

$$\mathbf{X} = X_{np} = \begin{bmatrix} x_{11} & x_{12} & \cdots & x_{1p} \\ x_{21} & x_{22} & \cdots & x_{2p} \\ \vdots & \vdots & \ddots & \vdots \\ x_{n1} & x_{n2} & \cdots & x_{np} \end{bmatrix} . \tag{3}$$

For EOF analysis performed on $\mathbf{X}$, the objective is to find the coefficients of the vector $\boldsymbol{\alpha}_1 = (\alpha_{11}, \ldots, \alpha_{1p})^{\mathrm{T}}$, where $(\cdot)^{\mathrm{T}}$ indicates the transpose, such that the sample variance of $\mathbf{b}_1 = \mathbf{X}\boldsymbol{\alpha}_1$

$$\frac{1}{n-1} \sum_{i=1}^{n} (b_{1i} - \bar{b}_1)^2 \tag{4}$$

is maximized. This procedure is repeated for $\mathbf{b}_2 = \mathbf{X}\boldsymbol{\alpha}_2$ through $\mathbf{b}_p = \mathbf{X}\boldsymbol{\alpha}_p$, with the stipulation that $\boldsymbol{\alpha}_k^{\mathrm{T}}\boldsymbol{\alpha}_k = 1$, and all $\mathbf{z}$ time series are uncorrelated. $\boldsymbol{\alpha}_k$ is referred to as the k^{th} EOF, and $\mathbf{b}_k$ is the corresponding principal component time series (or "score" series).

Finding the vectors $\boldsymbol{\alpha}_k$ gives rise to an eigenvalue problem as follows. The $p \times p$ covariance matrix $\mathbf{S}$ is

$$\mathbf{S} = \frac{1}{n-1}\mathbf{X}^{\mathrm{T}}\mathbf{X}\,. \tag{5}$$

The variance of $\mathbf{X}$ projected onto $\boldsymbol{\alpha}_k$ is

$$\mathrm{var}[\mathbf{X}\boldsymbol{\alpha}_k] = \frac{1}{n-1}(\mathbf{X}\boldsymbol{\alpha}_k)^{\mathrm{T}}(\mathbf{X}\boldsymbol{\alpha}_{\boldsymbol{k}}) = \boldsymbol{\alpha}_k^{\mathrm{T}}\mathrm{S}\boldsymbol{\alpha}_k\,, \tag{6}$$

and can be maximized subject to the orthogonality constraint $\boldsymbol{\alpha}_k^{\mathrm{T}}\boldsymbol{\alpha}_k = 1$ by introducing a Lagrange multiplier

$$\boldsymbol{\alpha}_k^{\mathrm{T}}\mathrm{S}\boldsymbol{\alpha}_k - \lambda\left[\boldsymbol{\alpha}_k^{\mathrm{T}}\boldsymbol{\alpha}_k - 1\right]. \tag{7}$$

Setting the derivative of (7) with respect to $\boldsymbol{\alpha}_k$ equal to zero yields

$$\mathbf{S}\boldsymbol{\alpha}_k = \lambda\boldsymbol{\alpha}_k\,, \tag{8}$$

showing that λ is an eigenvalue of $\mathbf{S}$ with corresponding eigenvector $\boldsymbol{\alpha}_k$. The largest λ maximizes $\boldsymbol{\alpha}_k^{\mathrm{T}}\mathbf{S}\boldsymbol{\alpha}_k = \boldsymbol{\alpha}_k^{\mathrm{T}}\lambda\boldsymbol{\alpha}_k = \lambda$.

While EOFs may be determined by solving (8) in terms of $\mathbf{S}$, performing a singular value decomposition (SVD) on the centered data matrix $\mathbf{X}$ is more computationally convenient.

The SVD of the $n \times p$ matrix $\mathbf{X}$ is

$$\mathbf{X} = \mathbf{A}\mathbf{\Sigma}\mathbf{U}^{\mathrm{T}}, \tag{9}$$

where $\mathbf{\Sigma}$ is a diagonal $p \times p$ matrix containing the singular values of $\mathbf{X}$ along its main diagonal, $\mathbf{A}$ is an $n \times p$ matrix with left singular vectors in its columns, $\mathbf{U}$ is an $p \times p$ matrix with right singular vectors in its columns, and p is the rank of $\mathbf{X}$. In addition, the columns of $\mathbf{A}$ and $\mathbf{U}$ are orthonormal, meaning $\mathbf{A}^{\mathrm{T}}\mathbf{A}$ and $\mathbf{U}^{\mathrm{T}}\mathbf{U}$ both result in the identity matrix $\mathbf{I}$.

The right singular vectors (columns of $\mathbf{U}$) are the eigenvectors of $\mathbf{S}$ and the EOFs of $\mathbf{X}$. The square roots of the eigenvalues lie along the diagonal of $\mathbf{\Sigma}$ and are ranked in descending order; hence, the first eigenvector explains the most variance in the data, the second explains the second largest amount of variance, and so forth. The left singular vectors (columns of $\mathbf{A}$) are the score series.

2.3.3 Computation of Complex Hilbert Empirical Orthogonal Functions

While traditional EOF analysis is useful for identifying the leading patterns, or modes, of variability within a data set, its inability to resolve propagating wave-like structures (Barnett, 1983) is a limitation. Complex Hilbert EOF (HEOF) analysis resolves propagating patterns by complexifying the input data so that its imaginary part is the original data set phase shifted in time by $\pi/2$ as described later in this subsection (Barnett, 1983; Horel, 1984; Hannachi et al., 2007). Here, HEOF analysis was applied separately to the detrended complexified

fields of $\tilde{C}$, $q\mathbf{v}$, *VA*, and *TA*. The components of $q\mathbf{v}$ were combined to form the $n \times 2p$ matrix

$$\mathbf{Q} = \begin{bmatrix} qu_{11} & \cdots & qu_{1p} & qv_{11} & \cdots & qv_{1p} \\ qu_{21} & \cdots & qu_{2p} & qv_{21} & \cdots & qv_{2p} \\ \vdots & \ddots & \vdots & \vdots & \ddots & \vdots \\ qu_{n1} & \cdots & qu_{np} & qv_{n1} & \cdots & qv_{np} \end{bmatrix}. \tag{10}$$

In addition, HEOF analysis was performed on the $n \times 2p$ matrices of the combined fields of $\tilde{C}$ and $q\mathbf{v}$, $\tilde{C}$ and *TA*, *VA* and *TA*, and *VA* and $q\mathbf{v}$. Thus, eight HEOF calculations were performed in total for three individual and five combined fields.

Since the variables have different units, the data were centered and standardized (i.e., the anomalies were divided by the standard deviation) to form a correlation matrix rather than a variance-covariance matrix, resulting in a singular value matrix Σ with correlation coefficients along the diagonal. The analysis domain extended from 20°N to 60°N and 60°W to 110°W on the $2.5° \times 2.5°$ NNR grid. The HEOFs were not rotated because the domain size was comparable to the scale of the circulation features of interest (Horel, 1981).

Following the notation in Hannachi et al. (2007), the standardized vector data field spanning times $t = 1, \ldots, n$ at p locations

$$\mathbf{x}_t = \left(x_{t1}, \cdots, x_{tp}\right)^{\mathrm{T}} \tag{11}$$

was complexified by the operation

$$\mathbf{y}_t = \mathbf{x}_t + i\mathscr{H}(\mathbf{x}_t)\,. \tag{12}$$

$\mathscr{H}(\cdot)$ denotes the Hilbert transform, which is defined as the Cauchy principal value of

$$\mathscr{H} \equiv \frac{1}{\pi}\int_{-\infty}^{\infty}\frac{f(t)}{(t-\tau)}d\tau\,. \tag{13}$$

$\mathbf{y}_t$ was then arranged in the $n \times p$ matrix

$$\mathbf{Y} = \left(y_t, \ldots, y_n\right)^{\mathrm{T}}\,. \tag{14}$$

As with traditional EOF analysis, the HEOFs were obtained from the SVD of the transformed complex correlation matrix

$$\mathbf{R} = \frac{1}{n-1}\mathbf{Y}^{*\mathrm{T}}\mathbf{Y}\,, \tag{15}$$

where $(\cdot)^*$ is the complex conjugate. The HEOFs

$$\mathbf{u}_k = \left(u_{k1}, \cdots, u_{kp}\right)^{\mathrm{T}}, k = 1, \ldots, p \tag{16}$$

are, thus, the eigenvectors of $\mathbf{R}$. The score series $\mathbf{z}_k = \mathbf{Y}\mathbf{u}_k$ is the projection of the data onto the k^{th} HEOF. Together, the real and imaginary parts of an HEOF provide a parsimonious representation of a propagating pattern that would otherwise appear as two degenerate patterns in quadrature in traditional EOF analysis (Hannachi et al., 2007). Here, it was verified

that the phases of the first two traditional EOFs of the individual and combined fields of the NNR variables were in quadrature.

2.3.4 Phase shift of complex Hilbert empirical orthogonal functions

Because it is complex, an HEOF has a spatial amplitude and phase, and its associated score series has a temporal amplitude and phase. Since the phase is arbitrary, the real and imaginary parts of an HEOF may by themselves depict patterns with little or no clear relevance to variations at a fixed location like the Midwest. The HEOFs are thus phase-shifted by the amount ϕ_k that maximizes the correlation between the real score series and the precipitation time series. This differs from the method in von Storch et al. (1988), which effectively maximizes the magnitude of the real part of the HEOF, and minimizes the magnitude of imaginary part of the HEOF without using the correlations of each part with an external variable.

The phase-shifted HEOF and associated PC are defined as

$$\tilde{\mathbf{u}}_k \equiv e^{-i\phi_k}\mathbf{u}_k \tag{17}$$

$$\tilde{\mathbf{z}}_k \equiv \mathbf{Y}\tilde{\mathbf{u}}_k \,. \tag{18}$$

The Voronoi weighted precipitation time series in vector form is

$$\mathbf{P} = \left(p_1, \cdots, p_n\right)^{\mathrm{T}}, \tag{19}$$

and the scalar complex correlation between $\mathbf{P}$ and $\tilde{\mathbf{z}}_k$ is

$$h_k \equiv \frac{(\mathbf{P}-\bar{\mathbf{P}})^T(\tilde{\mathbf{z}}_k-\bar{\tilde{\mathbf{z}}}_k)}{[(\mathbf{P}-\bar{\mathbf{P}})^T(\mathbf{P}-\bar{\mathbf{P}})(\tilde{\mathbf{z}}_k-\bar{\tilde{\mathbf{z}}}_k)^T(\tilde{\mathbf{z}}_k-\bar{\tilde{\mathbf{z}}}_k)]^{1/2}}\,, \tag{20}$$

where $\bar{\mathbf{P}}$ and $\bar{\tilde{\mathbf{z}}}_k$ are $n \times 1$ vectors containing the means of $\mathbf{P}$ and $\tilde{\mathbf{z}}_k$, respectively. Here, the order of computation of the numerator is important, as $(\tilde{\mathbf{z}}_k-\bar{\tilde{\mathbf{z}}}_k)^{*\mathrm{T}}(\mathbf{P}-\bar{\mathbf{P}})$ yields the complex conjugate of h_k. It can be seen from (17) and (18) that h_k depends on ϕ_k, meaning that maximizing the real part of h_k will produce the desired phase shift. Considering that the correlation of $\mathbf{P}$ and $\tilde{\mathbf{z}}_k$ is

$$f_k = h_k e^{-i\phi_k} = \mathrm{Re}(h_k)\cos\phi_k - \mathrm{Im}(h_k)\sin\phi_k\,, \tag{21}$$

where $\mathrm{Re}(\cdot)$ is the real part and $\mathrm{Im}(\cdot)$ is the imaginary part, differentiating (21) with respect to ϕ_k and setting the result to zero

$$\frac{\partial \mathrm{Re}(f_k)}{\partial \phi_k} = -\mathrm{Re}(h_k)\sin\phi_k - \mathrm{Im}(h_k)\cos\phi = 0, \tag{22}$$

yields the critical point

$$\check{\phi}_k = \arctan\left[-\frac{\mathrm{Im}(h_k)}{\mathrm{Re}(h_k)}\right]; -\frac{\pi}{2} < \check{\phi}_k < \frac{\pi}{2}; \mathrm{Re}(h_k) \neq 0\,. \tag{23}$$

If the second derivative of $\mathrm{Re}(h_k) < 0$ at $\breve{\phi}_k$, then $\breve{\phi}_k$ is a local maximum and

$$\frac{\partial^2 \mathrm{Re}(h_k)}{\partial {\phi_k}^2} = -\cos\breve{\phi}_k \frac{\mathrm{Re}(h_k)^2 + \mathrm{Im}(h_k)^2}{\mathrm{Re}(h_k)}\,, \tag{24}$$

resulting in the phase shift

$$\phi_k = \begin{cases} \breve{\phi}_k & \text{if } \mathrm{Re}(h_k) > 0\,, \\ \breve{\phi}_k + \pi & \text{if } \mathrm{Re}(h_k) < 0\,, \end{cases} \tag{25}$$

since $\cos\breve{\phi}_k > 0$ for $(-\pi/2, \pi/2)$.

To illustrate the utility of the phase shift ϕ_k, the leading HEOF of DJF $q\mathbf{v}$ is considered as an example. Prior to the application of the phase shift in (17) and (18), the leading HEOF of $q\mathbf{v}$ depicts a cyclonic circulation centered over the Midwest in the real part (Fig. 5a), and northeasterly $q\mathbf{v}$ over the domain in the imaginary part (Fig. 5b). Most of the the absolute value, or modulus, of the correlation between the unshifted HEOF ($\phi_1 = 0$) and $P^{0.25}$ is comprised of the imaginary part ($\mathrm{Im}(h_1)$; Fig. 6, white square), and the negative sign on $\mathrm{Im}(h_1)$ is expected because the imaginary part of the unshifted HEOF (Fig. 5b) depicts relatively dry flow from the Midwest toward the moisture source in the Gulf of Mexico. $\mathrm{Re}(h_1)$ (Fig. 6, gray square) has a smaller magnitude because the real part of the unshifted HEOF (Fig. 5a) depicts weak $q\mathbf{v}$ with an anticyclonic circulation centered over the Midwest.

While the proportion of each part that contributes to the modulus depends on ϕ_k, the modulus itself does not. Therefore, shifting the phase of this HEOF such that the correlation

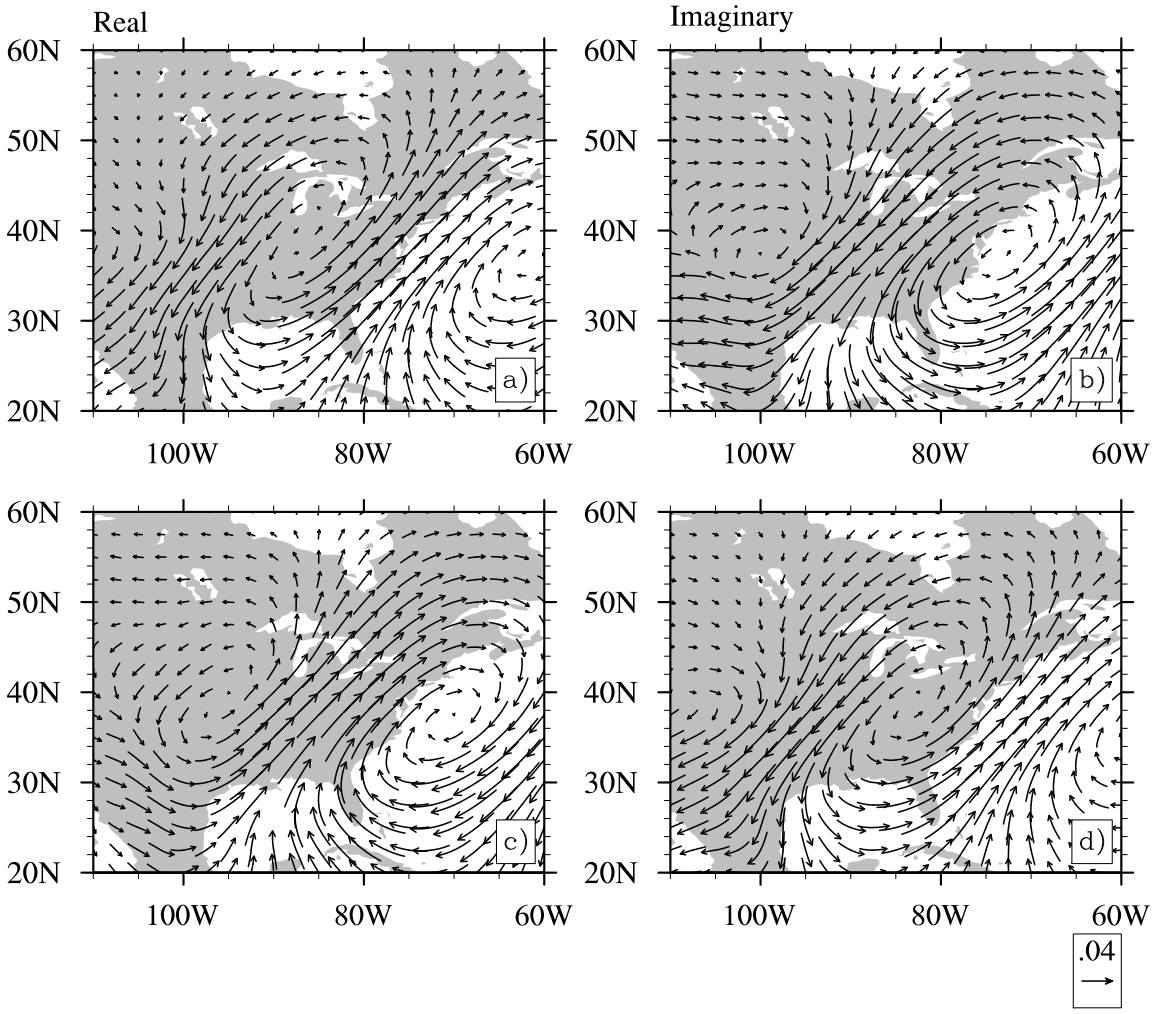

Fig. 5: For the leading HEOF of DJF $q\mathbf{v}$: a) the real and b) the imaginary part prior to phase shifting, c) the real and d) the imaginary part of the phase-shifted HEOF. Units are standardized.

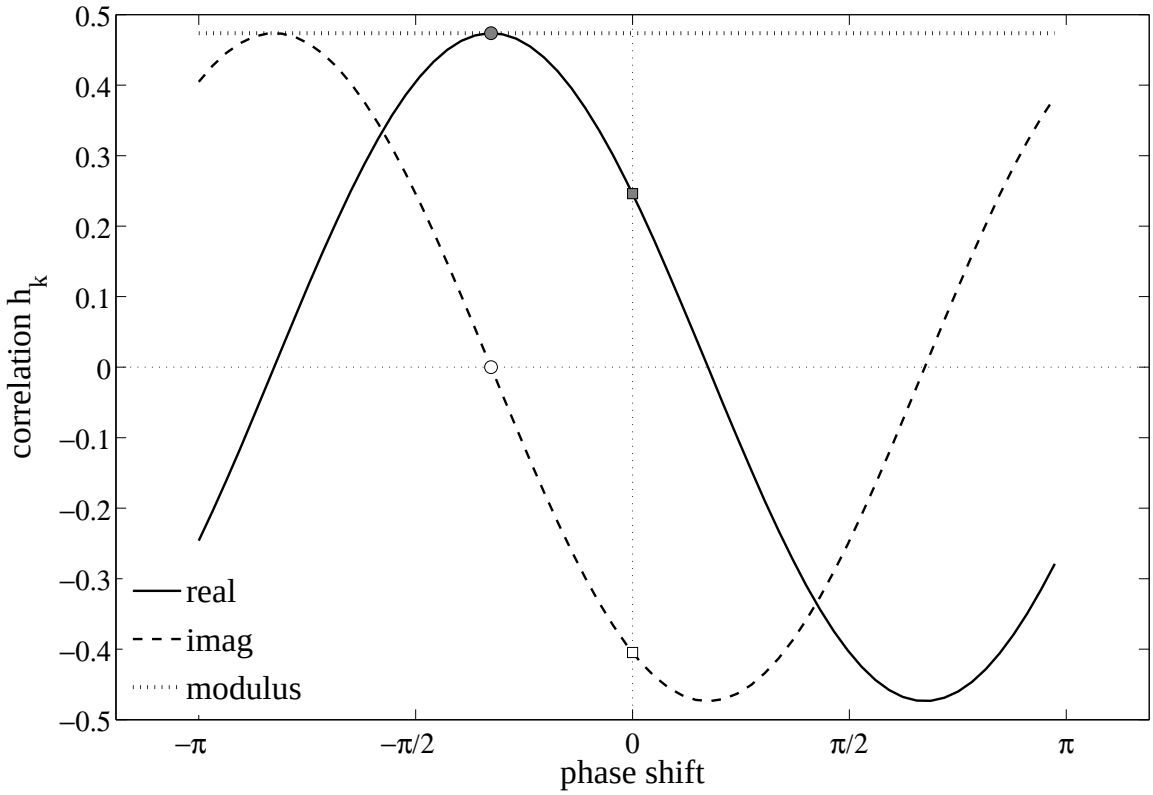

Fig. 6: Real (solid line) and imaginary (dashed line) parts of the correlation between $P^{0.25}$ and the leading HEOF of DJF $q\mathbf{v}$ as a function of the phase shift ϕ_1. The dotted line indicates the modulus correlation. Gray and white squares indicate the real and imaginary parts of the correlation prior to phase-shifting. Circles denote the real and imaginary parts of the correlation with phase shift $\phi_1 = -0.33\pi$.

between DJF precipitation and the real part of the score series is maximized simplifies interpretation of the HEOF, as all of the explanatory power of DJF precipitation resides in the real part. In this example, the desired phase shift is $\phi_1 = -0.33\pi$ (Fig. 6, gray circle). Centered between an upstream cyclone and downstream anticyclone, moist southerly 850-hPa flow is present over much of the Midwest in the real part of the HEOF (Fig. 5c), which accounts for 45% of the variance in DJF $P^{0.25}$. Since the imaginary part has zero correlation with DJF $P^{0.25}$ (Fig. 6, white circle), it is statistically irrelevant, serving only to indicate the propagation of the pattern. All HEOFs in this thesis were phase-shifted to maximize their real correlation with $P^{0.25}$, and only the real parts of the phase-shifted HEOFs are shown in subsequent sections for patterns with relatively simple eastward propagation like those in Fig. 5. For patterns with other types of propagation (e.g., meridional), the real and imaginary parts are shown.

CHAPTER 3

RESULTS AND DISCUSSION

3.1 Composite fields

Composite anomalies of the NNR-based variables for days with heavy precipitation, defined here as precipitation in the 90th percentile of all days, for DJF, MAM, JJA, and SON provide a first-order assessment of the large-scale environment on days with heavy precipitation. The exit sector of an upper-level trough is present over the Midwest (Fig. 7) with the largest positive $\tilde{C}$ anomalies centered northeast of the Great Lakes in DJF, MAM, and SON. $q\mathbf{v}$ vectors depict a cyclonic circulation upstream of the Midwest and a downstream anticyclonic circulation in all seasons, though the pattern is somewhat weaker in JJA.

Anomalous positive *TA* over the Midwest and strong cyclonic *VA* anomalies upstream (Fig. 8) also define the 90th-percentile environment. As before, this pattern persists throughout all seasons, but is weaker in JJA, particularly with regard to the positive *VA* anomaly over the central U.S. Composite anomalies of 90th-percentile 850-hPa wind vectors (Fig. 9) are similar to the composite anomalies of $q\mathbf{v}$, depicting southerly or southwesterly flow over the Midwest between an upstream cyclonic circulation and downstream anticyclonic circulation in all seasons. Positive column-total precipitable water anomalies are present over the Midwest as well (Fig. 9), indicating the presence of high atmospheric moisture content

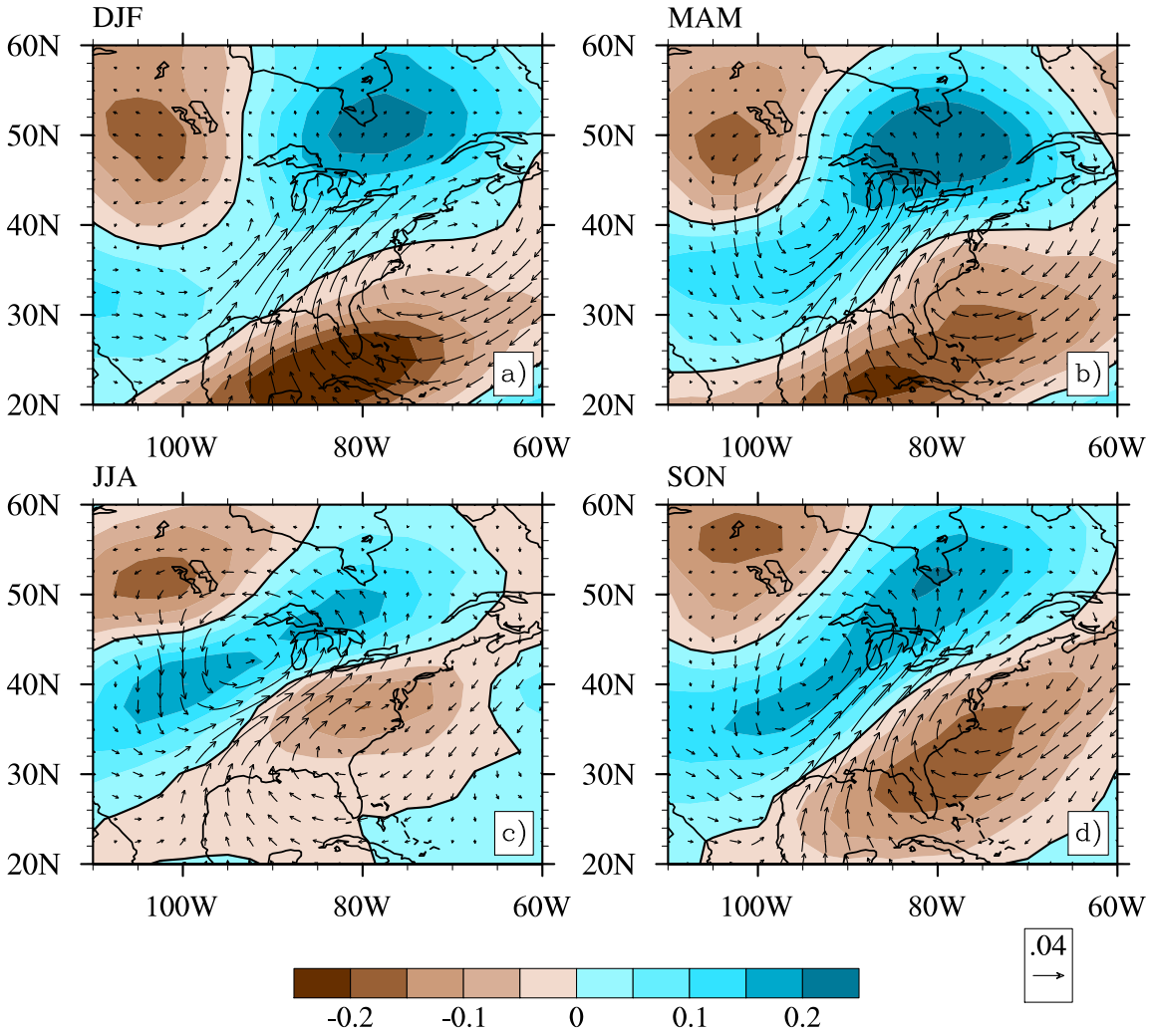

Fig. 7: Composite anomalies of $\tilde{C}$ (shaded contours) and $q\mathbf{v}$ (kg kg^{-1}m s^{-1}, arrows) on days with $P^{0.25}$ in the 90th percentile for a) DJF, b) MAM, c) JJA, and d) SON. The zero contour is in bold.

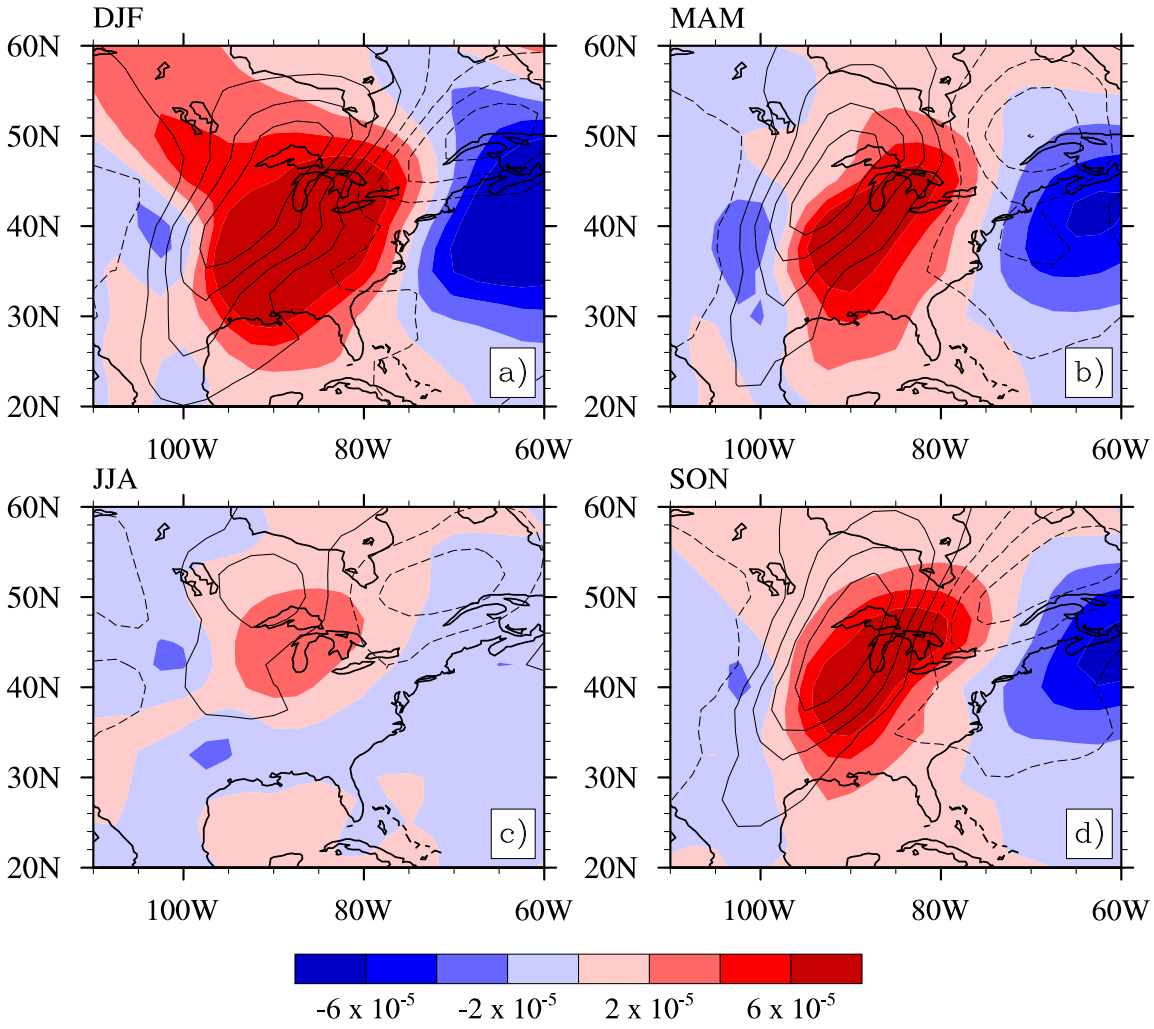

Fig. 8: Composite anomalies of *VA* (s^{-2}, contours) and *TA* (K s^{-1}, shading) on days with $P^{0.25}$ in the 90th percentile for a) DJF, b) MAM, c) JJA, and d) SON. Dashed contours indicate negative values, solid contours indicate positive values, and the zero contour is in bold. The contour interval for *VA* is 0.4×10^{-9} s^{-2}.

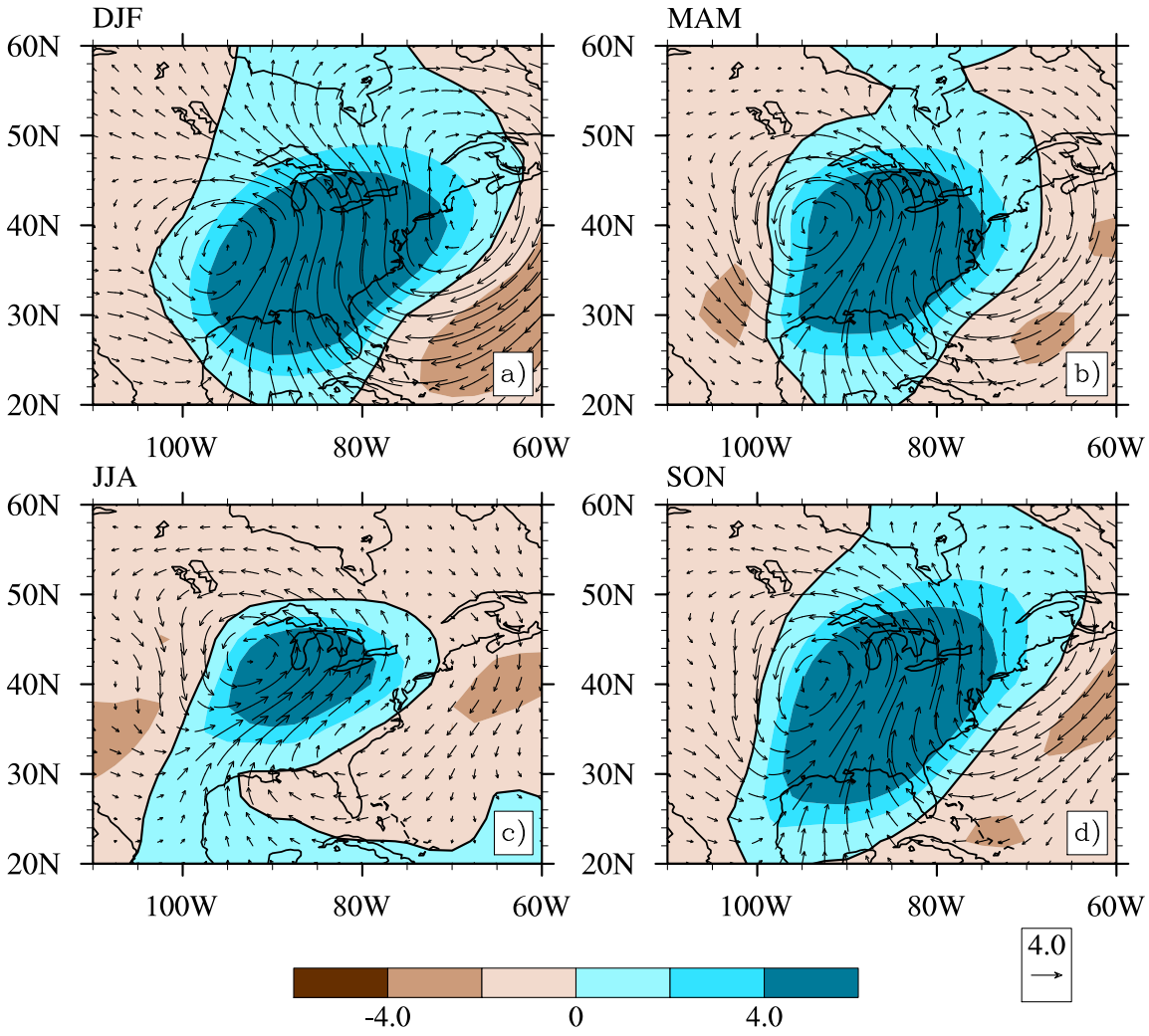

Fig. 9: Composite anomalies of column total precipitable water (kg m^{-2}, shaded contours) and 850-hPa wind (m s^{-1}, arrows) on days with $P^{0.25}$ in the 90th percentile for a) DJF, b) MAM, c) JJA, and d) SON. The zero contour is in bold.

that is necessary for heavy precipitation. Using $q\mathbf{v}$ as a proxy for atmospheric moisture rather than preciptable water is advantageous because it shows the pattern in the 850-hPa wind field, and indicates the source region of the moisture in the Gulf of Mexico.

Overall, the 90th-percentile patterns depict large-scale dynamics that favor precipitation. The increased likelihood of a jet suggests the presence of a synoptic cyclone and/or jet streak which, when combined with sufficient atmospheric moisture, can enhance precipitation. Likewise, positive *TA* and *VA* anomalies are indicative of increased instability and rising motion in the vicinity of the Midwest, as in the presence of an upstream trough, which may generate heavy precipitation.

By contrast, composite anomalies for dry days, defined as those with $P^{0.25}$ in the 10th percentile, show conditions the opposite of those for 90th percentile precipitation days. Negative $\tilde{C}$ anomalies and a low-level anticyclonic circulation are located upstream of the Midwest (Fig. 10). Northeasterly $q\mathbf{v}$ indicates the predominantly northerly flow and relative lack of moisture over the center of the domain (Fig. 11). These features occur in conjunction with anticyclonic *VA* located upstream of *TA* minima over the Midwest (Fig. 12).

3.2 The annual cycle of Midwest precipitation

EOF or HEOF analysis often begins with the removal of the seasonal cycle through filtering, or focusing on individual seasons. Prior to separate-season analyses (section 3.3), a year-round view is presented to illustrate the role of propagating patterns in the annual cycle. The configuration of the real and imaginary parts in Fig. 13a,b indicates that the leading HEOF (HEOF1) of combined $\tilde{C}$ and $q\mathbf{v}$ is a largely meridionally-propagating pattern, and accounts for 16% of the variance in the combined field (Table 1). Year-round HEOF1

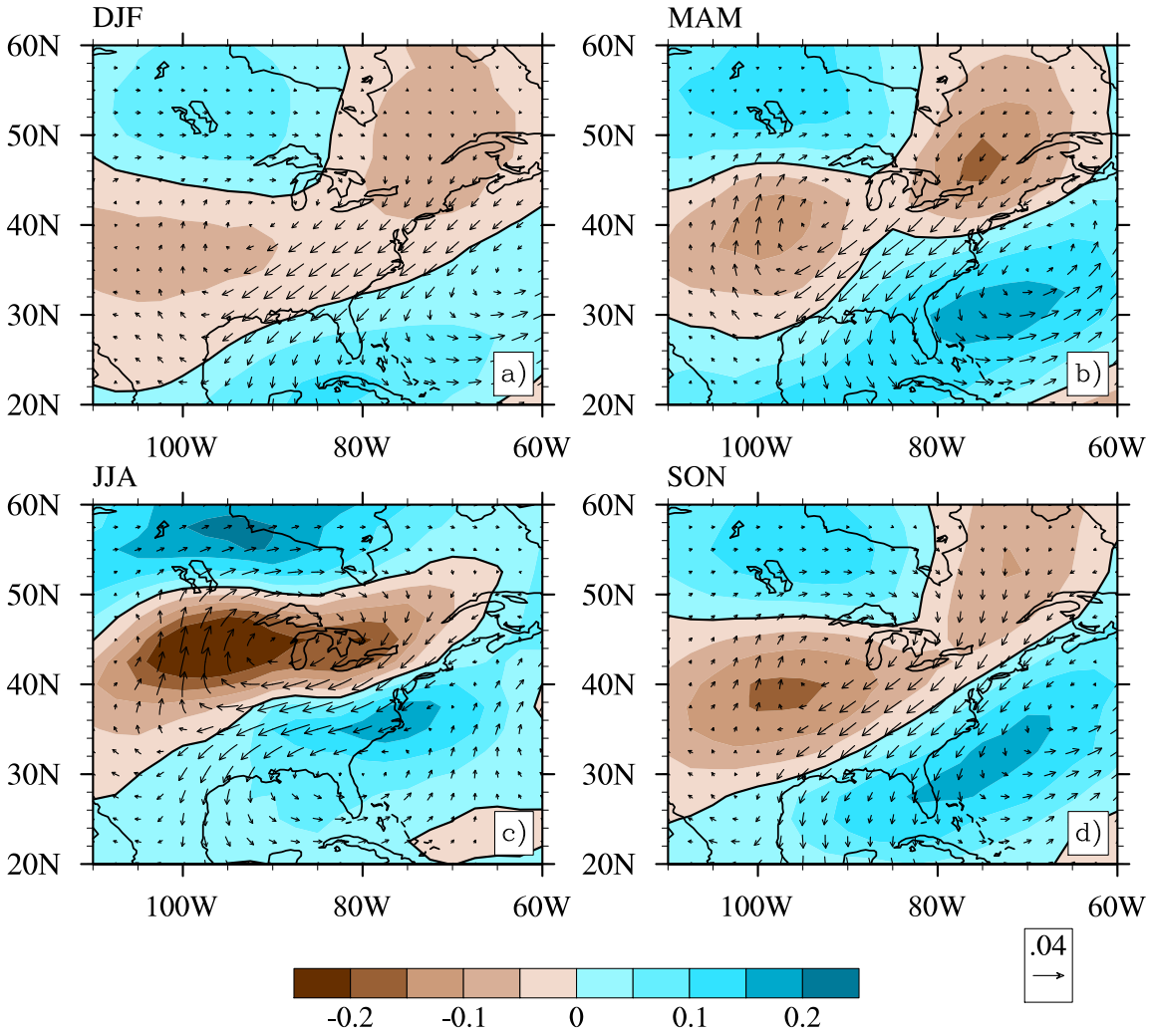

Fig. 10: Composite anomalies of $\tilde{C}$ (shaded contours) and $q\mathbf{v}$ (kg kg^{-1}m s^{-1}, arrows) on days with $P^{0.25}$ in the 10th percentile for a) DJF, b) MAM, c) JJA, and d) SON. The zero contour is in bold.

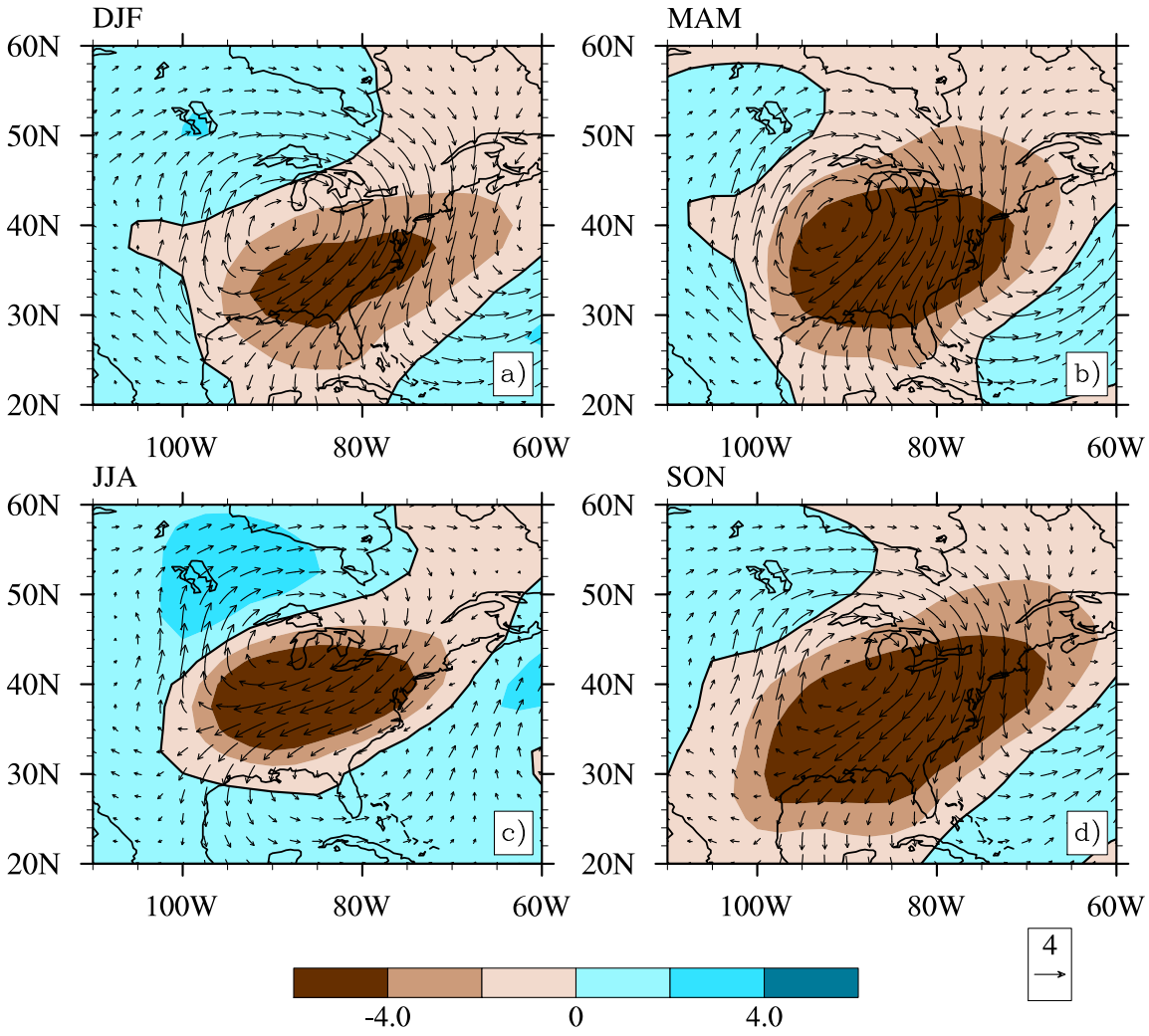

Fig. 11: Composite anomalies of column total precipitable water (kg m^{-2}, shaded contours) and 850-hPa wind (m s^{-1}, arrows) on days with $P^{0.25}$ in the 10th percentile for a) DJF, b) MAM, c) JJA, and d) SON. The zero contour is in bold.

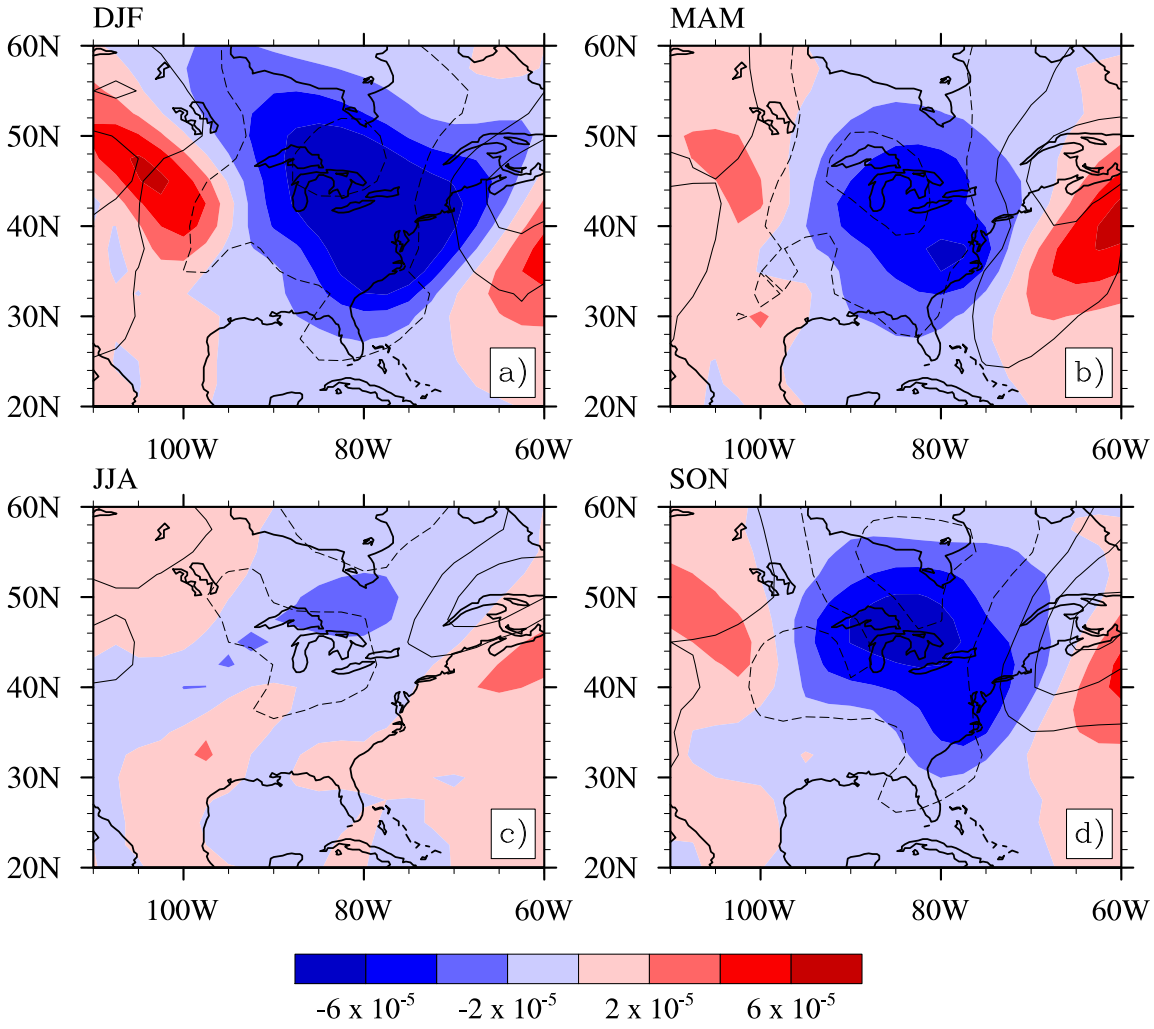

Fig. 12: Composite anomalies of *VA* (s^{-2}, contours) and *TA* (K s^{-1}, shading) on days with $P^{0.25}$ in the 15th percentile for a) DJF, b) MAM, c) JJA, and d) SON. Dashed contours indicate negative values, solid contours indicate positive values, and the zero contour is in bold. The contour interval for *VA* is 0.4×10^{-9} s^{-2}.

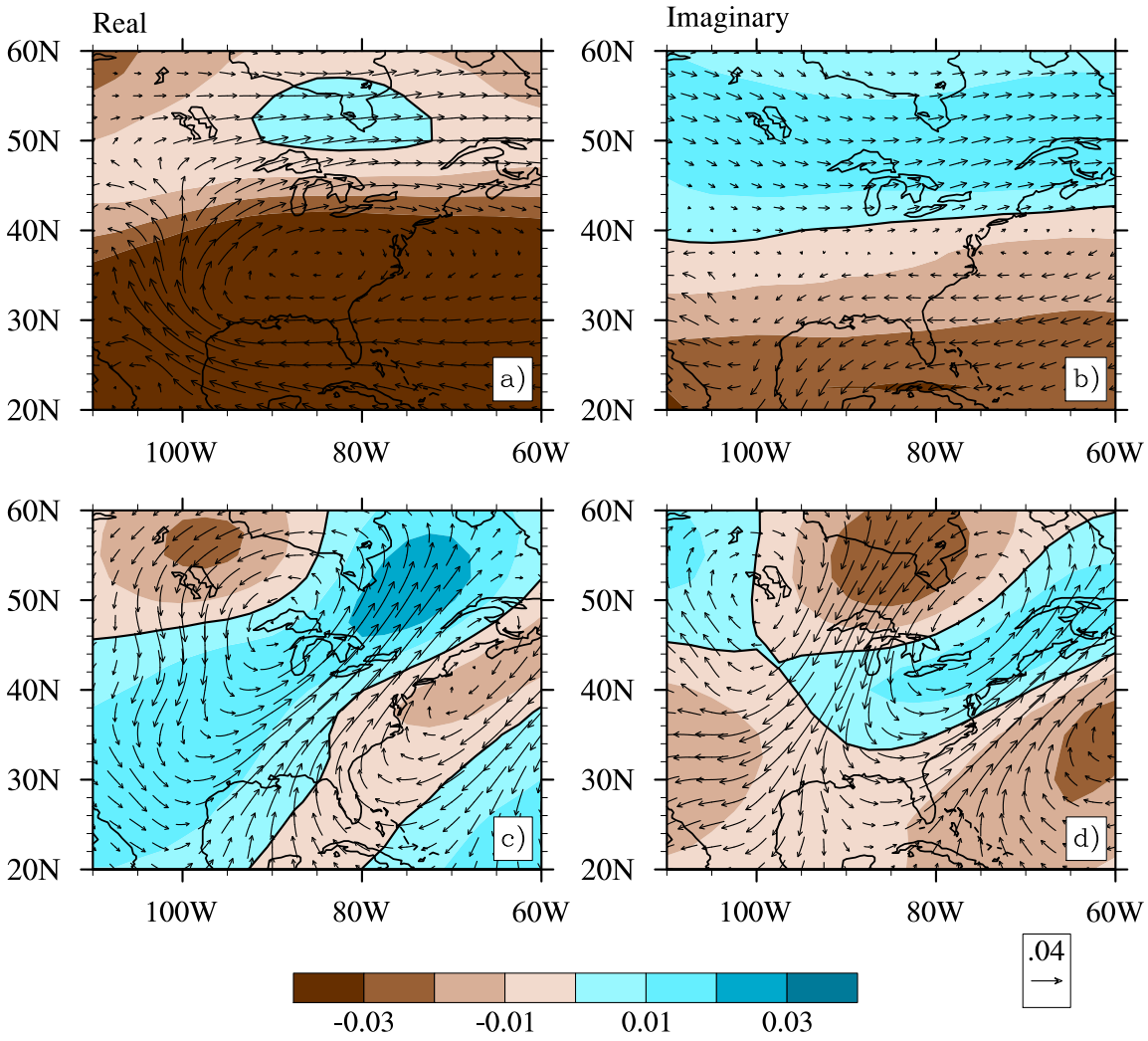

Fig. 13: The real and imaginary parts of HEOF1 and HEOF2 of combined $\tilde{C}$ (shaded contours) and $q\mathbf{v}$ (arrows). a) and b) correspond to HEOF1. c) and d) correspond to HEOF2.

Table 1: Percent of the variance explained by the first three HEOFs of the year-round NNR-derived variables.

HEOF	$q\mathbf{v}$	$\tilde{C}$	TA	VA	$\tilde{C}$, $q\mathbf{v}$	$\tilde{C}$, TA	VA, $q\mathbf{v}$	VA, TA
1	15	29	17	12	16	16	12	12
2	11	10	8	5	10	9	8	5
3	9	7	6	5	7	5	7	4

of combined $\tilde{C}$ and $q\mathbf{v}$ will be referred to as the "annual cycle HEOF". The annual cycle score series (Fig. 14a) clearly shows that this pattern follows the seasonal cycle of jet stream migration shown in Fig. 4, with positive scores during the summer months reflecting the northward displacement of the jet stream and enhanced moist southerly flow (Fig. 4c), and negative scores corresponding to the opposite winter scenario (Fig. 4a).

The second HEOF (HEOF2) of combined $\tilde{C}$ and $q\mathbf{v}$ (Fig. 13c,d) accounts for 10% of the variance in the combined field (Table 1), and strongly resembles the "storm" pattern of the composite anomaly fields in Fig. 7. Year-round HEOF2 of combined $\tilde{C}$ and $q\mathbf{v}$ will be referred to as the "storm HEOF". Though the storm HEOF score series exhibits a large amount of noise, scores are generally negative in the summer and positive in the winter, indicative of the seasonal shift in the high-frequency variability associated with synoptic waves. Together, the annual cycle and storm HEOFs account for approximately 25% of the variance in the combined field, and are well-separated according to the North criteria (North et al., 1982). The correlation coefficients between the annual cycle and storm HEOFs and daily precipitation are 0.25 and 0.57, respectively.

High-frequency variability was removed from the annual cycle and storm HEOF score series by computing the long-term weekly means (Fig. 15). Like the daily scores (Fig. 14), long-term weekly mean annual cycle HEOF scores (Fig. 15b) are positive in JJA and negative in DJF. The long-term weekly mean storm HEOF scores (Fig. 15c) are generally positive in winter and summer, but tend to be negative during early-mid fall. Long-term weekly mean $P^{0.25}$ (Fig. 15a) closely follows the long-term weekly mean annual cycle HEOF scores (Fig. 15b), and the variance is generally aligned with the variance in the long-term weekly mean storm HEOF scores (Fig. 15c).

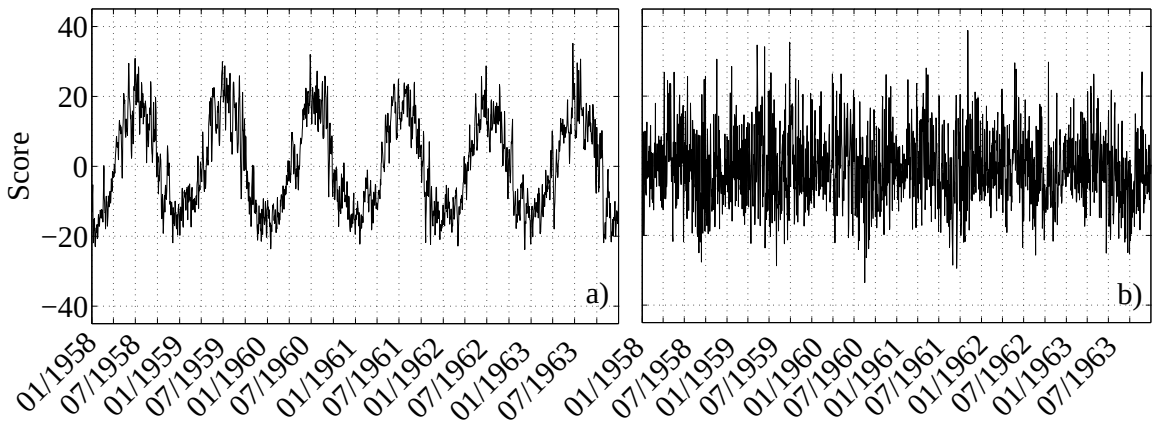

Fig. 14: Jan 1958–Dec 1963 of the score series of a) HEOF1 and b) HEOF2 of combined $\tilde{C}$ and $q\mathbf{v}$. Ticks are every Jan 1, Apr 1, Jul 1, and Oct 1.

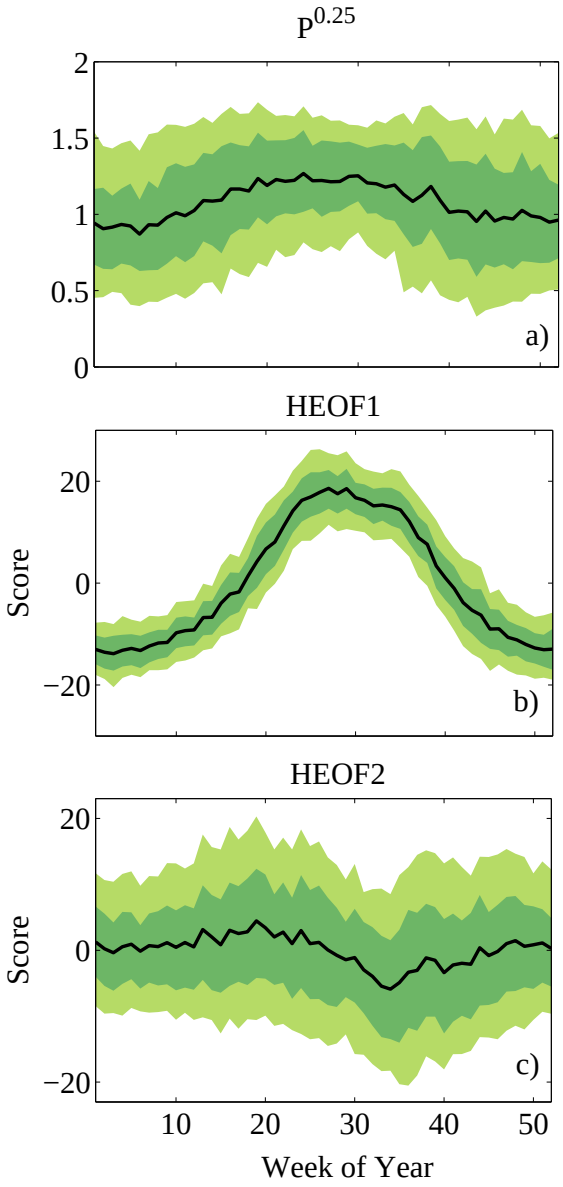

Fig. 15: Bold curves show the long-term weekly time series of the mean of a) $P^{0.25}$, b) HEOF1, and c) HEOF2 of the combined $\tilde{C}$ and $q\mathbf{v}$ fields. Light green shading defines areas within the 10th and 90th percentiles. Dark green shading defines areas within the 25th and 75th percentiles.

The long-term weekly mean and variance of the annual cycle HEOF scores were retained as predictors in a backward stepwise regression onto long-term weekly mean $P^{0.25}$ (statistically significant at $\alpha = 0.05$), and accounted for 69% of the variance in the regression. However, the significant correlation between the long-term weekly variance of the storm HEOF and long-term weekly mean precipitation (Table 2) indicates that the storm HEOF is also an important component of the annual cycle of Midwest precipitation. In early-mid fall, negative long-term weekly mean storm HEOF scores indicate that the field of combined $\tilde{C}$ and $q\mathbf{v}$ projects negatively onto the pattern in Fig. 13c,d. Thus, $\tilde{C}$ values must be small or negative, and/or $q\mathbf{v}$ must have dominant northerly component over the center of the domain.

Since the variance of the long-term weekly mean storm HEOF scores is positively correlated with long-term weekly mean $P^{0.25}$, and most of the explanatory power of the storm HEOF results from $q\mathbf{v}$, it is unlikely that negative long-term weekly mean storm HEOF scores result from predominantly negative $q\mathbf{v}$. Rather, the negative storm HEOF scores probably reflect the tendency for strong southerly low-level moisture transport and a low occurrence of a jet over the Midwest in the fall.

3.3 Within-season Midwest precipitation variability

3.3.1 Relationship with jet stream probability and horizontal moisture transport

In all seasons, HEOF1 of combined $\tilde{C}$ and $q\mathbf{v}$ (Fig. 16) captures the $\tilde{C}$ pattern and propagating low-level cyclone-anticyclone couplet present in the 90$^{\text{th}}$-percentile composite anomalies. HEOF1 of combined $\tilde{C}$ and $q\mathbf{v}$ also resembles the storm HEOF from the year-long analysis (Fig. 13c,d).

Table 2: Correlation coefficients of the long-term weekly means and variances of year-round combined $\tilde{C}$ and $q\mathbf{v}$ HEOF scores and $P^{0.25}$. Mean is abbreviated "mn" and variance is abbreviated "var". Bold values are statistically significant at $\alpha = 0.05$.

	$P^{0.25}$ mn	$P^{0.25}$ var	HEOF1 mn	HEOF1 var	HEOF2 mn	HEOF2 var
$P^{0.25}$ mn	1					
$P^{0.25}$ var	**-0.559**	1				
HEOF1 mn	**0.563**	0.062	1			
HEOF1 var	**0.906**	**-0.567**	**0.522**	1		
HEOF2 mn	-0.006	-0.006	0.048	**-0.334**	1	
HEOF2 var	**0.622**	0.126	**0.762**	**0.665**	-0.220	1

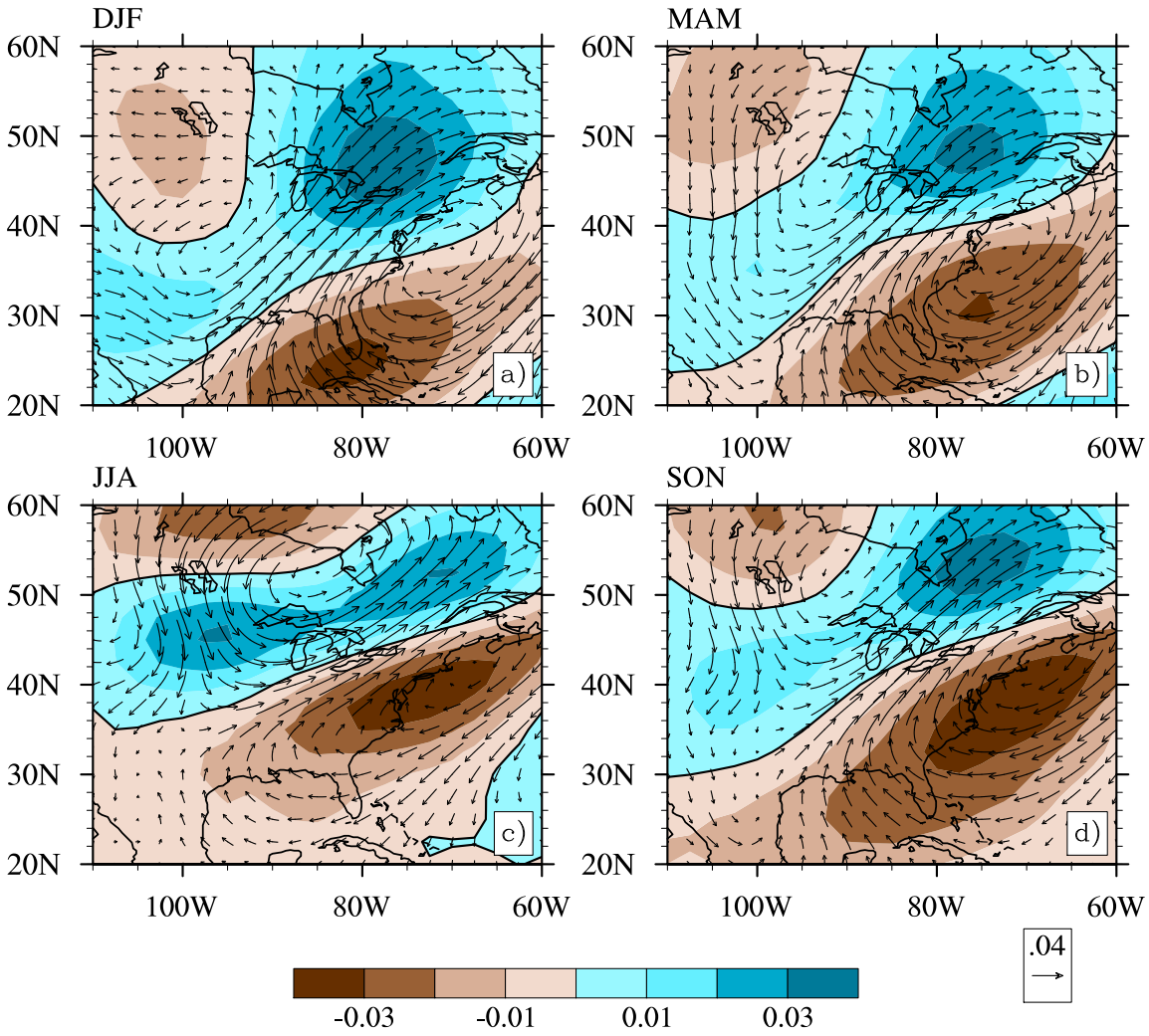

Fig. 16: HEOF1 of combined $\tilde{C}$ (shaded contours) and $q\mathbf{v}$ (arrows) for a) DJF, b) MAM, c) JJA, and d) SON. The zero contour is in bold.

In DJF, MAM, and JJA, $P^{0.25}$ has the greatest correlation with the combined $\tilde{C}$ and $q\mathbf{v}$ HEOF1 score series (Table 3). Correlations are strongest in DJF and MAM and weakest in JJA. In other words, the pattern that explains the most variance (Table 4) in combined $\tilde{C}$ and $q\mathbf{v}$ in JJA is a poor estimate of precipitation variability, even though similar HEOFs have comparatively robust relationships with precipitation in other seasons and the regressions are all statistically significant ($\alpha = 0.05$). The seasonal variation in the relationship between HEOF1 of $\tilde{C}$ and $q\mathbf{v}$ and Midwest precipitation is visible in scatter plots (Fig. 17). Stratification of $P^{0.25}$ in the scatter plots likely results from subjective bias in precipitation amounts reported at Cooperative Observer Program (COOP) stations (Daly et al., 2007).

HEOF1 of $q\mathbf{v}$ alone (Fig. 18) is nearly identical to the $q\mathbf{v}$ field in HEOF1 of combined $\tilde{C}$ and $q\mathbf{v}$. Both HEOFs are similarly correlated with $P^{0.25}$ (Table 3), indicating that most of the explanatory power in the combined field of $\tilde{C}$ and $q\mathbf{v}$ is derived from $q\mathbf{v}$. HEOF1 of $\tilde{C}$ alone (Fig. 19) resembles the annual cycle HEOF from the year-round analysis (Fig. 13a,b), and has a low correlation with $P^{0.25}$ in all seasons (Table 3). HEOF2 of $\tilde{C}$ alone resembles the storm HEOF from the year-round analysis (Fig. 13c,d) in DJF (Fig. 20a) and SON (Fig. 20d). However, MAM (Fig. 20b) and JJA (Fig. 20c) are characterized by a zonal jet over the central U.S., which is accompanied by ridging in JJA.

3.3.2 Relationship with vorticity advection and temperature advection

The leading HEOF of combined *VA* and *TA* (Fig. 21) captures aspects of a propagating synoptic wave. The loadings are similar to the composite anomalies in Fig. 8, except that the local maximum in warm advection is somewhat broader and oriented more north-south

Table 3: Correlation coefficients of precipitation and the leading HEOFs of the within-season NNR-derived variables. All values are statistically significant at $\alpha = 0.05$.

	DJF									MAM								
	$P^{0.25}$	$q\mathbf{v}$	$\tilde{C}$	*TA*	*VA*	$\tilde{C}$, $q\mathbf{v}$	$\tilde{C}$, *TA*	*VA*, $q\mathbf{v}$	*VA*, *TA*	$P^{0.25}$	$q\mathbf{v}$	$\tilde{C}$	*TA*	*VA*	$\tilde{C}$, $q\mathbf{v}$	$\tilde{C}$, *TA*	*VA*, $q\mathbf{v}$	*VA*,*TA*
$P^{0.25}$	1									1								
$q\mathbf{v}$	0.670	1								0.663	1							
$\tilde{C}$	0.132	0.179	1							0.248	0.240	1						
TA	0.571	0.825	0.047	1						0.576	0.807	0.147	1					
VA	0.471	0.750	0.078	0.757	1					0.495	0.719	0.100	0.726	1				
$\tilde{C}$, $q\mathbf{v}$	0.674	0.986	0.285	0.806	0.736	1				0.673	0.977	0.400	0.775	0.672	1			
$\tilde{C}$, *TA*	0.590	0.817	0.149	0.955	0.749	0.835	1			0.618	0.797	0.447	0.911	0.655	0.846	1		
VA, $q\mathbf{v}$	0.653	0.986	0.158	0.852	0.848	0.969	0.843	1		0.652	0.977	0.200	0.841	0.841	0.943	0.807	1	
VA, *TA*	0.565	0.852	0.070	0.959	0.909	0.834	0.928	0.911	1	0.577	0.831	0.134	0.945	0.909	0.788	0.857	0.908	1
	JJA									.1								
	$P^{0.25}$	$q\mathbf{v}$	$\tilde{C}$	*TA*	*VA*	$\tilde{C}$, $q\mathbf{v}$	$\tilde{C}$, *TA*	*VA*, $q\mathbf{v}$	*VA*, *TA*	$P^{0.25}$	$q\mathbf{v}$	$\tilde{C}$	*TA*	*VA*	$\tilde{C}$, $q\mathbf{v}$	$\tilde{C}$, *TA*	*VA*, $q\mathbf{v}$	*VA*,*TA*
$P^{0.25}$	1									1								
$q\mathbf{v}$	0.406	1								0.579	1							
$\tilde{C}$	0.226	0.324	1							0.180	0.187	1						
TA	0.316	0.586	0.121	1						0.569	0.756	0.181	1					
VA	0.318	0.451	0.085	0.561	1					0.444	0.650	0.068	0.600	1				
$\tilde{C}$, $q\mathbf{v}$	0.426	0.972	0.479	0.536	0.404	1				0.564	0.957	0.392	0.749	0.600	1			
$\tilde{C}$, *TA*	0.377	0.685	0.603	0.723	0.403	0.774	1			0.534	0.692	0.551	0.862	0.555	0.819	1		
VA, $q\mathbf{v}$	0.412	0.981	0.283	0.674	0.583	0.937	0.703	1		0.595	0.978	0.159	0.800	0.787	0.926	0.707	1	
VA, *TA*	0.357	0.610	0.112	0.926	0.817	0.555	0.668	0.731	1	0.563	0.781	0.150	0.945	0.879	0.754	0.801	0.870	1

Table 4: Percent of variance explained by the first three HEOFs of the within-season NNR-derived variables.

	DJF								MAM							
HEOF	$q\mathbf{v}$	$\tilde{C}$	*TA*	*VA*	$\tilde{C}$, $q\mathbf{v}$	$\tilde{C}$, *TA*	*VA*, $q\mathbf{v}$	*VA*, *TA*	$q\mathbf{v}$	$\tilde{C}$	*TA*	*VA*	$\tilde{C}$, $q\mathbf{v}$	$\tilde{C}$, *TA*	*VA*, $q\mathbf{v}$	*VA*,*TA*
1	20	17	19	14	15	12	16	15	17	15	16	13	13	10	14	13
2	9	10	8	5	8	9	7	5	10	11	8	6	9	7	7	5
3	8	8	7	5	7	6	6	4	8	8	6	5	7	6	6	4
	JJA								SON							
HEOF	$q\mathbf{v}$	$\tilde{C}$	*TA*	*VA*	$\tilde{C}$, $q\mathbf{v}$	$\tilde{C}$, *TA*	*VA*, $q\mathbf{v}$	*VA*, *TA*	$q\mathbf{v}$	$\tilde{C}$	*TA*	*VA*	$\tilde{C}$, $q\mathbf{v}$	$\tilde{C}$, *TA*	*VA*, $q\mathbf{v}$	*VA*,*TA*
1	14	12	10	8	11	8	11	7	16	18	17	13	13	12	13	13
2	9	10	6	5	7	7	6	4	9	11	8	6	9	9	7	5
3	8	7	5	4	6	5	5	3	8	8	5	4	7	6	6	4

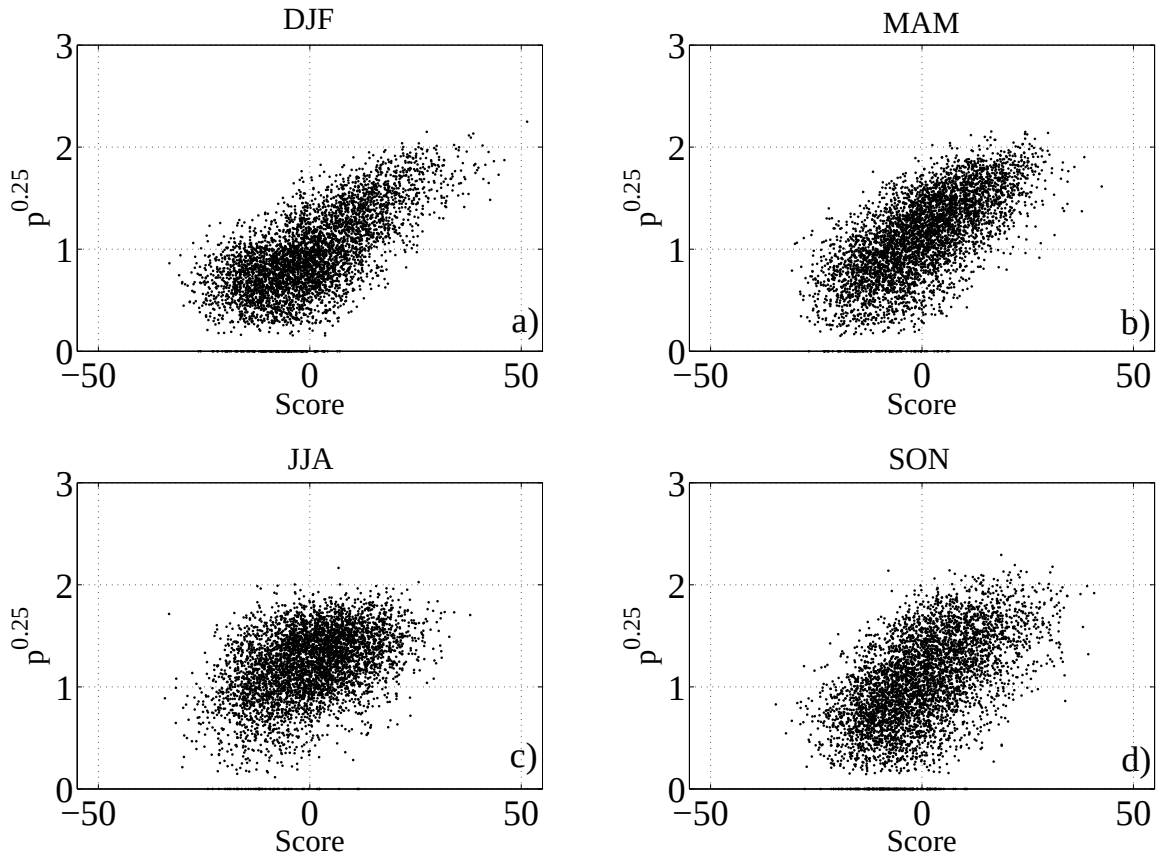

Fig. 17: Scatter plots of $P^{0.25}$ ($mm^{0.25}$) vs. score series for HEOF1 of combined $\tilde{C}$ and $q\mathbf{v}$ for a) DJF, b) MAM, c), JJA, and d) SON.

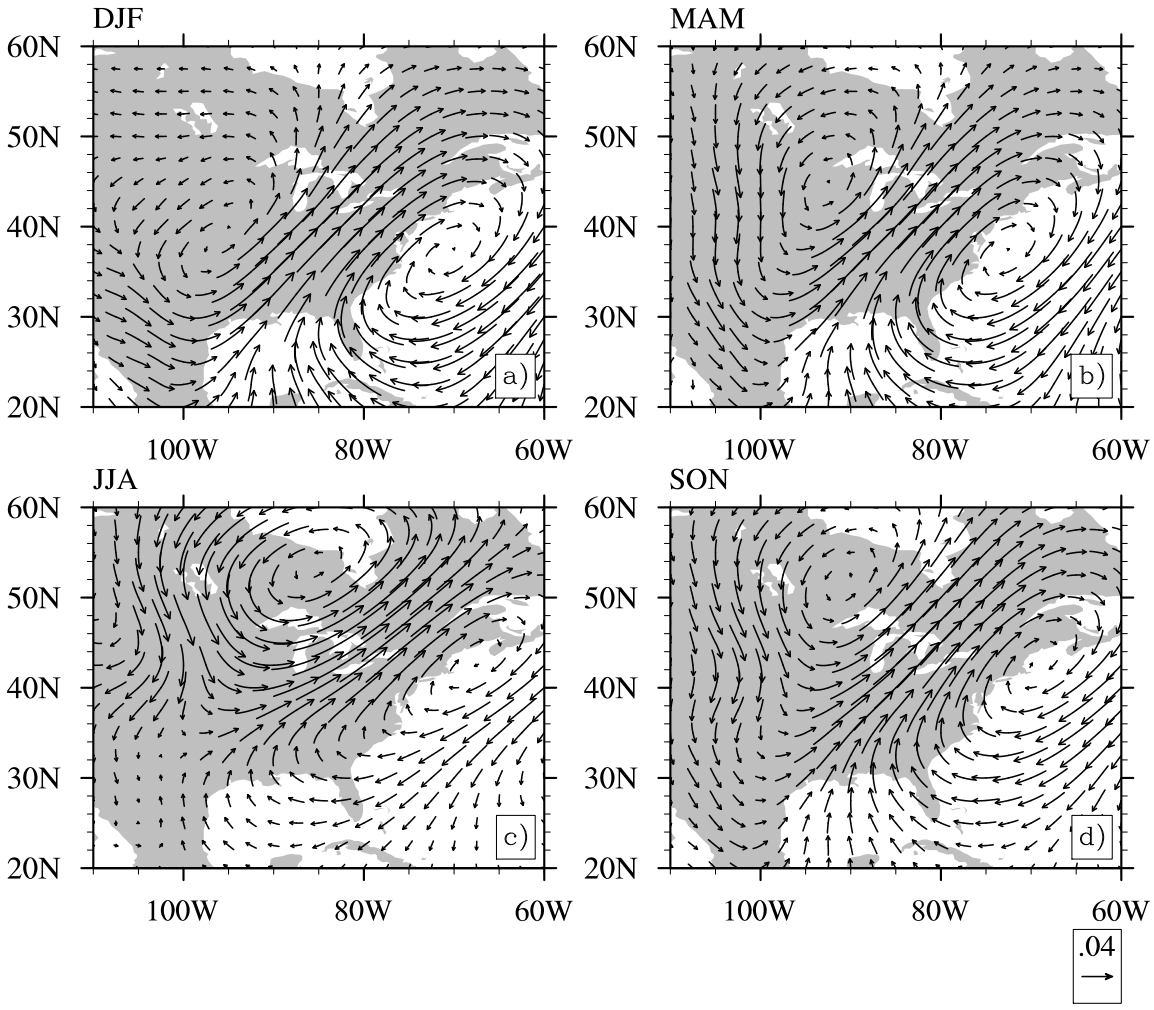

Fig. 18: HEOF1 of $q\mathbf{v}$ for a) DJF, b) MAM, c) JJA, and d) SON.

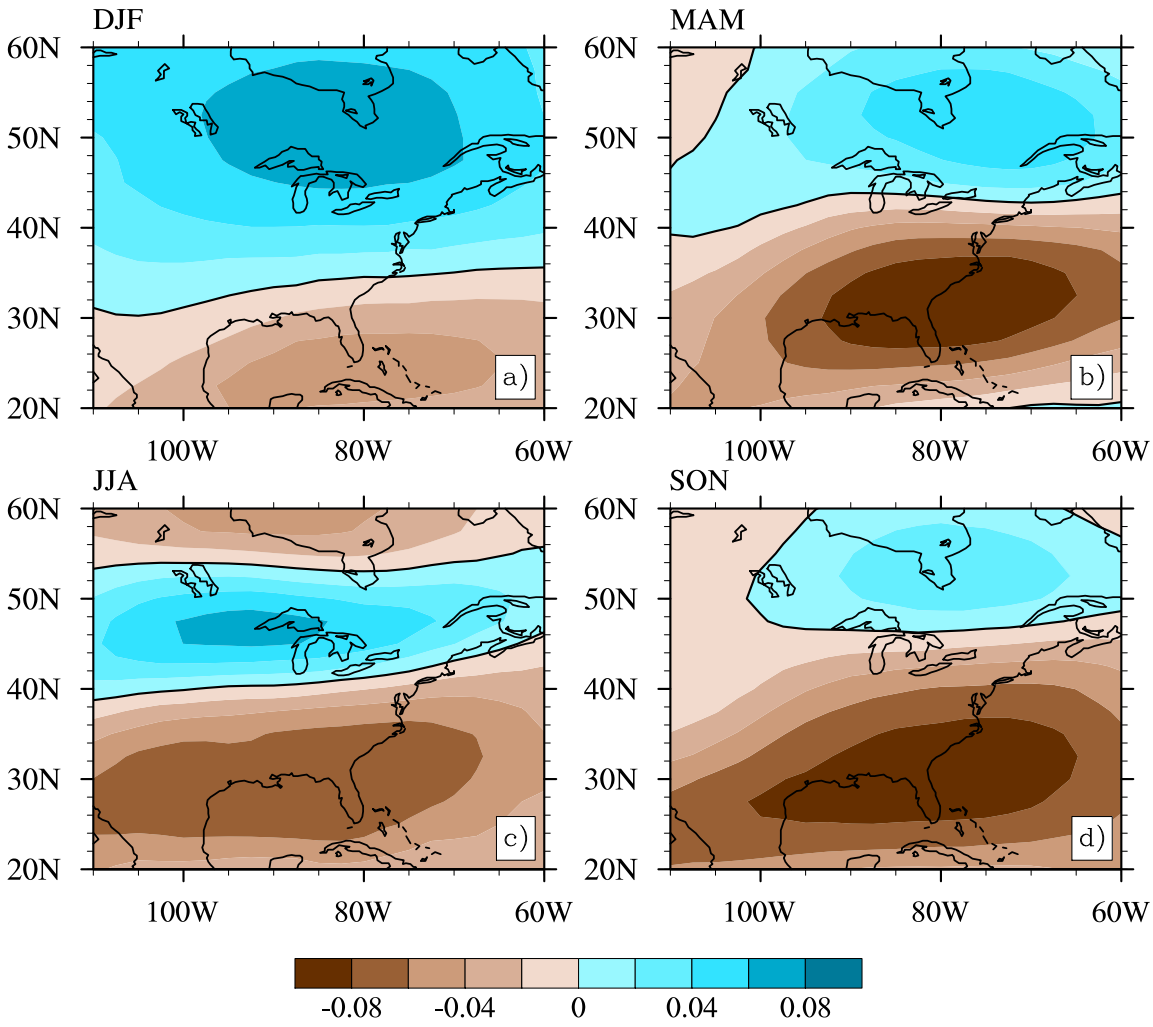

Fig. 19: HEOF1 of $\tilde{C}$ for a) DJF, b) MAM, c) JJA, and d) SON.

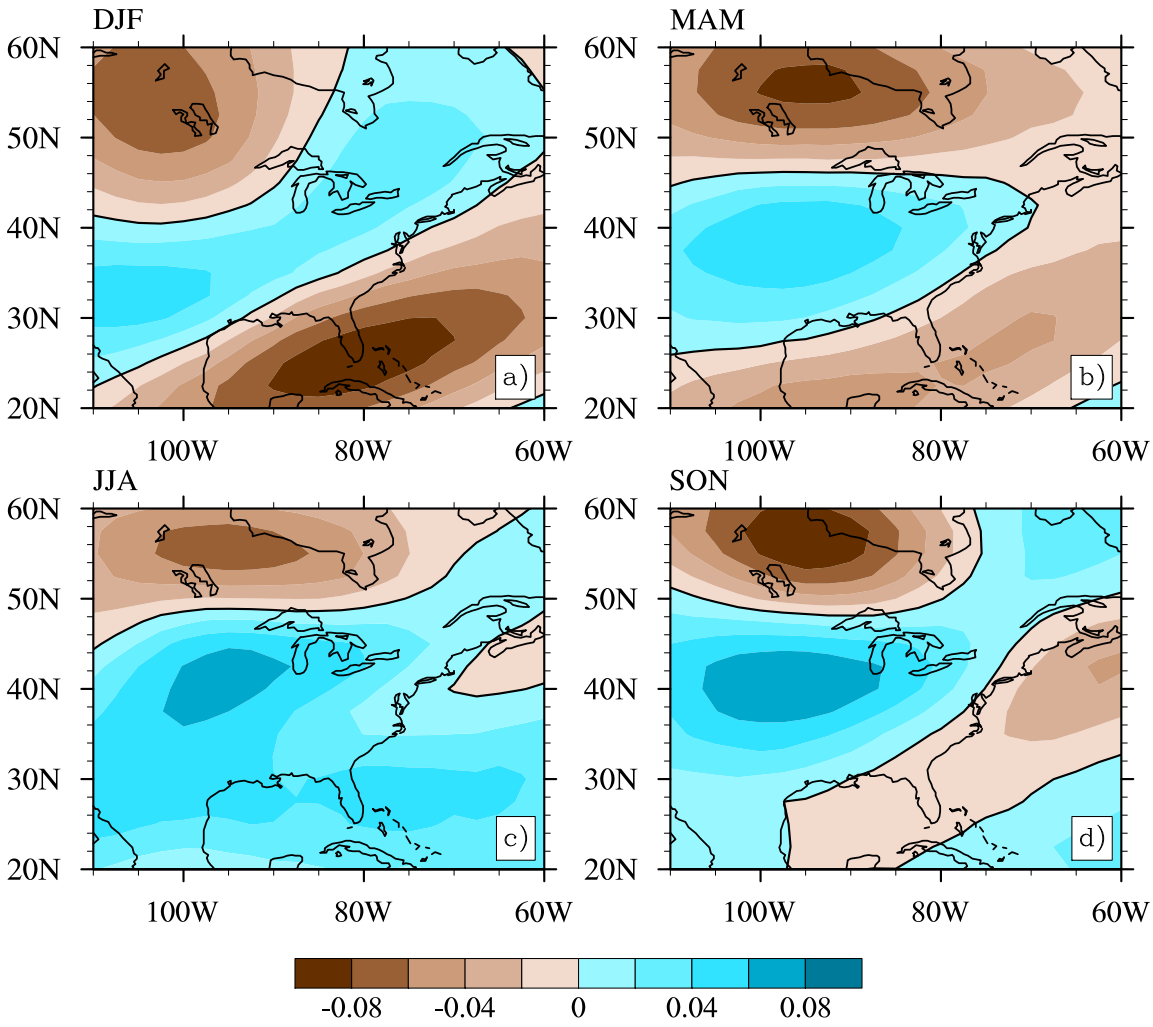

Fig. 20: HEOF2 of $\tilde{C}$ for a) DJF, b) MAM, c) JJA, and d) SON.

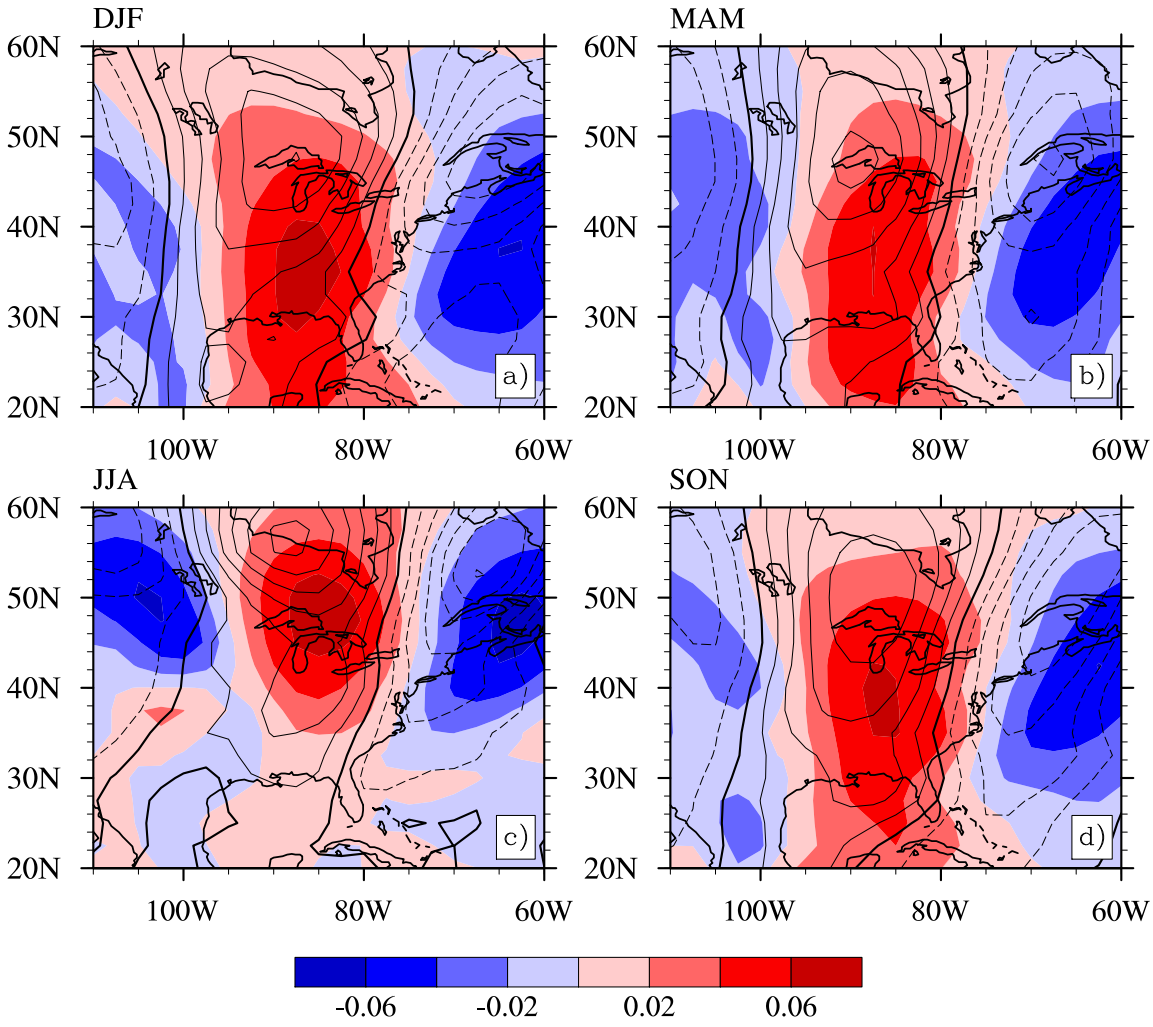

Fig. 21: HEOF1 of combined *VA* (contours) and *TA* (shaded contours) for a) DJF, b) MAM, c) JJA, and d) SON. Dashed contours indicate negative values, solid contours indicate positive values, and the zero *VA* contour is in bold. The contour interval for *VA* is 0.01.

in the HEOFs. The center of warm advection is also displaced slightly north of the 90th-percentile location in JJA. In DJF, MAM, and JJA, HEOF1 of combined *VA* and *TA* has a lower correlation with $P^{0.25}$ than the leading HEOF of combined $\tilde{C}$ and $q\mathbf{v}$ (Table 3). In SON, $P^{0.25}$ is similarly correlated with all leading HEOFs except HEOF1 of $\tilde{C}$ and HEOF1 of *VA*.

3.3.3 Relationship with teleconnections

The PNA is one of the leading modes of variability in the winter Northern Hemisphere 500-hPa height field (Wallace and Gutzler, 1981). The positive phase of the PNA depicts a wave train consisting of an anomalously strong Aleutian Low, positive height anomalies over the western U.S., and negative height anomalies over the southeastern U.S. Both the PNA and the MEI are significantly correlated with HEOF1 of combined $\tilde{C}$ and $q\mathbf{v}$ (Table 5) and precipitation (Table 6) during DJF, which may reflect a connection between the PNA and the El Niño-Southern Oscillation (ENSO) phenomena (e.g., Namias et al., 1988; Trenberth, 1990; Bladé, 1999; Hannachi, 2010), though disagreement exists regarding the strength and nature of this connection. However neither the PNA nor the MEI explain as much variability in DJF Midwest precipitation as HEOF1 of $q\mathbf{v}$ (Table 6).

The correlation between the PNA and DJF $P^{0.25}$ is in agreement with the results of Leathers et al. (1991), which showed correlations ranging from about -0.40 to -0.50 between the PNA and winter precipitation over the Midwest. Additionally, Rodiionov (1994) found that composites of the 700-hPa height field for 14 winters with very high and very low precipitation over the Great Lakes strongly resembled the positive and negative phases of the PNA pattern, respectively. Coleman and Rogers (2003) also found that monthly mean

Table 5: Correlations between monthly mean values of within-season HEOF1 of combined $\tilde{C}$ and $q\mathbf{v}$ score series and teleconnection indices. Bold values are statistically significant at $\alpha = 0.05$.

	Teleconnection		
	NAO	PNA	MEI
DJF	**0.245**	**-0.455**	**-0.332**
MAM	0.095	**-0.215**	-0.064
JJA	-0.072	-0.136	0.022
SON	**0.138**	-0.093	-0.057

Table 6: Correlations between monthly mean $P^{0.25}$ and teleconnection indices. Correlations between monthly mean $P^{0.25}$ and HEOF1 of combined $\tilde{C}$ and $q\mathbf{v}$ are shown in the last column. Bold values are statistically significant at $\alpha = 0.05$.

	Teleconnection			
	NAO	PNA	MEI	HEOF1 of $\tilde{C}$ and $q\mathbf{v}$
DJF	**0.155**	**-0.407**	**-0.227**	**0.614**
MAM	-0.059	**-0.229**	0.052	**0.530**
JJA	**-0.268**	0.037	0.144	**0.486**
SON	-0.014	**-0.188**	0.064	**0.462**

precipitation in the Ohio River Valley (ORV), most of which lies in the southeastern part of the Midwest domain, is linked to the PNA during DJF. Defining the "ORV Index" as the average standardized precipitation anomaly over all stations, the authors found that the meridional component of 850-hPa moisture flux, denoted $\overline{qv}$, was significantly greater over the ORV for winters in the upper-most quintile of the ORV index compared to winters in the lowest quintile. Furthermore, the pattern of the $q\mathbf{v}$ vectors in HEOF1 of combined $\tilde{C}$ and $q\mathbf{v}$ mirrors that of $\overline{qv}$ during the wettest winters, which has an axis oriented southwest–northeast extending from the Gulf of Mexico to the eastern U.S.

The propagating wave associated with HEOF1 of combined $\tilde{C}$ and $q\mathbf{v}$ (Fig. 16) projects onto the trough upstream of the Midwest defined in the negative phase of the PNA (Wallace and Gutzler, 1981, their Fig. 16). The centers of action in the $\tilde{C}$ field (Fig. 16a) are located between the maximum and minimum in 500-hPa height anomalies over the U.S. in the negative phase of the PNA (Wallace and Gutzler, 1981, their Fig. 16), as the enhanced height gradient between the upstream trough and downstream ridge implies the presence of a jet stream. This is in agreement with Strong and Davis (2008), which found that the negative phase of the second EOF of winter Northern Hemisphere extratropical $\tilde{C}$ anomalies, characterized by a merged jet stream over central North America, is associated with the negative phase of the PNA. However, HEOF1 of combined $\tilde{C}$ and $q\mathbf{v}$ is more highly correlated with Midwest precipitation than the PNA, the MEI , or the NAO in all seasons (Table 6) perhaps because it captures patterns associated with propagating regional waves rather than hemispheric standing waves.

3.4 Winter variability

Though HEOF1 of combined $\tilde{C}$ and $q\mathbf{v}$ is a reasonable estimate of daily DJF precipitation, the linear regression accounts for only about 45% of the variance in DJF $P^{0.25}$. This results in part because the HEOF analysis does not fully resolve mesoscale processes like lake effect snow that occur during the winter. Because the domain includes stations near Lake Michigan, Lake Superior, and Lake Huron, lake effect snow contributes to DJF precipitation.

Lake effect snow in the Great Lakes region often occurs following the passage of an upper-level trough, which typically results in low-level north or northwesterly flow over the lake surface. Provided that the lake is unfrozen, and that surface to 850-hPa lapse rate is about 10°–13°C (e.g, E. W. Holroyd, 1971; Niziol et al., 1995), cold advection over the lake results in upward heat and moisture fluxes, favoring the development of clouds and precipitation (e.g., Rothrock, 1969; R.R. Braham, 1983); thus, the characteristics of a lake effect snow environment in the Great Lakes region are effectively opposite those shown in HEOF1 of combined $\tilde{C}$ and $q\mathbf{v}$. Additionally, these conditions (i.e., $q\mathbf{v}$ vectors pointing south, southeast, or even southwest over the Great Lakes) are not depicted in the subsequent four HEOFs.

Because the synoptic environment in which lake effect snow occurs is quite different from the one that favors precipitation from mid-latitude cyclones, it is possible that a lake effect pattern is present on days with large negative combined $\tilde{C}$ and $q\mathbf{v}$ HEOF1 scores. Not surprisingly, anomalies for days in DJF with the 9 highest combined $\tilde{C}$ and $q\mathbf{v}$ HEOF1 scores (Figs. 22 and 23) generally resemble Figs. 7 and 8, with positive $\tilde{C}$ anomalies, south-southwesterly $q\mathbf{v}$, 850-hPa warm advection, and cyclonic *VA* over the Midwest. The 9 lowest combined $\tilde{C}$ and $q\mathbf{v}$ HEOF1 scores (Figs. 24 and 25) correspond to days with nonzero

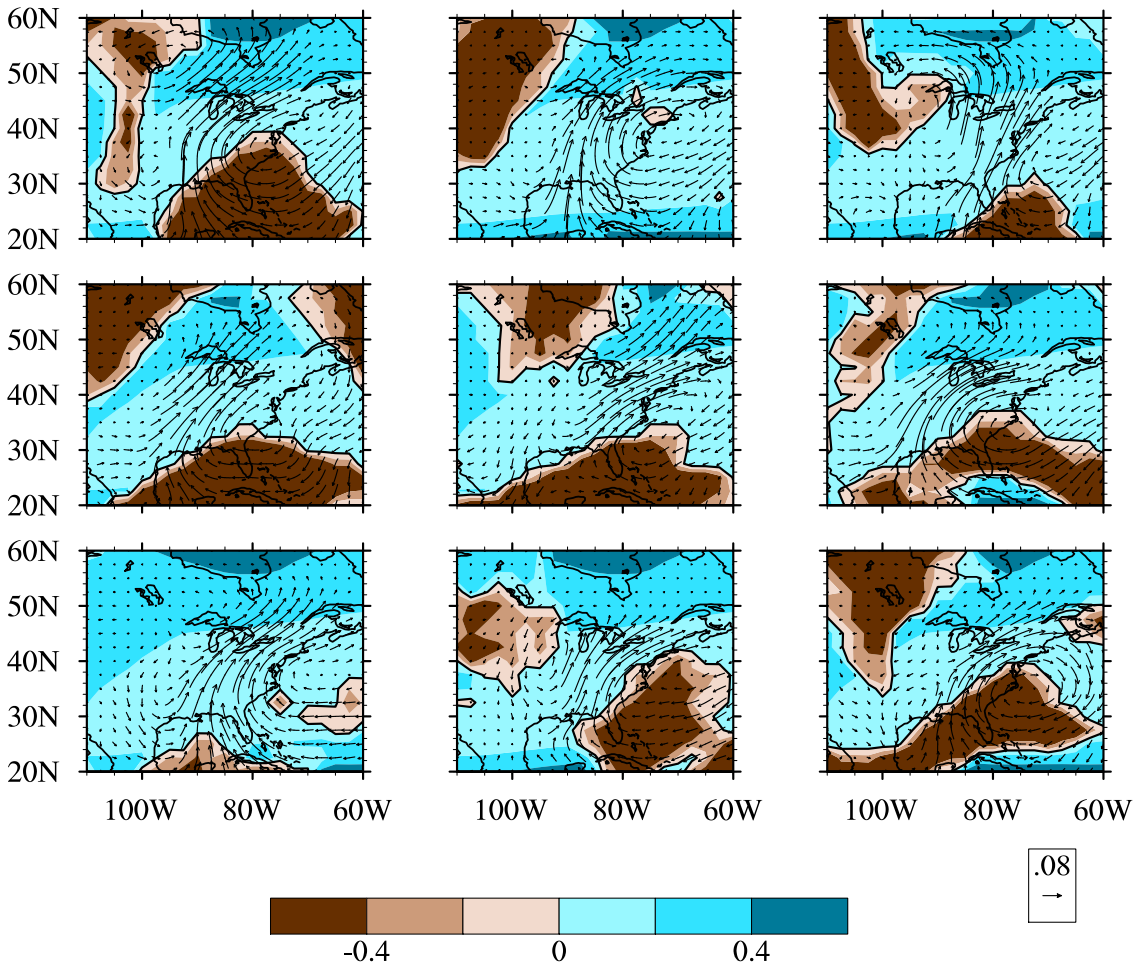

Fig. 22: $\tilde{C}$ (shaded contours) and $q\mathbf{v}$ (arrows) on the days with the 9 highest combined $\tilde{C}$ and $q\mathbf{v}$ HEOF1 scores in DJF. The zero contour is in bold.

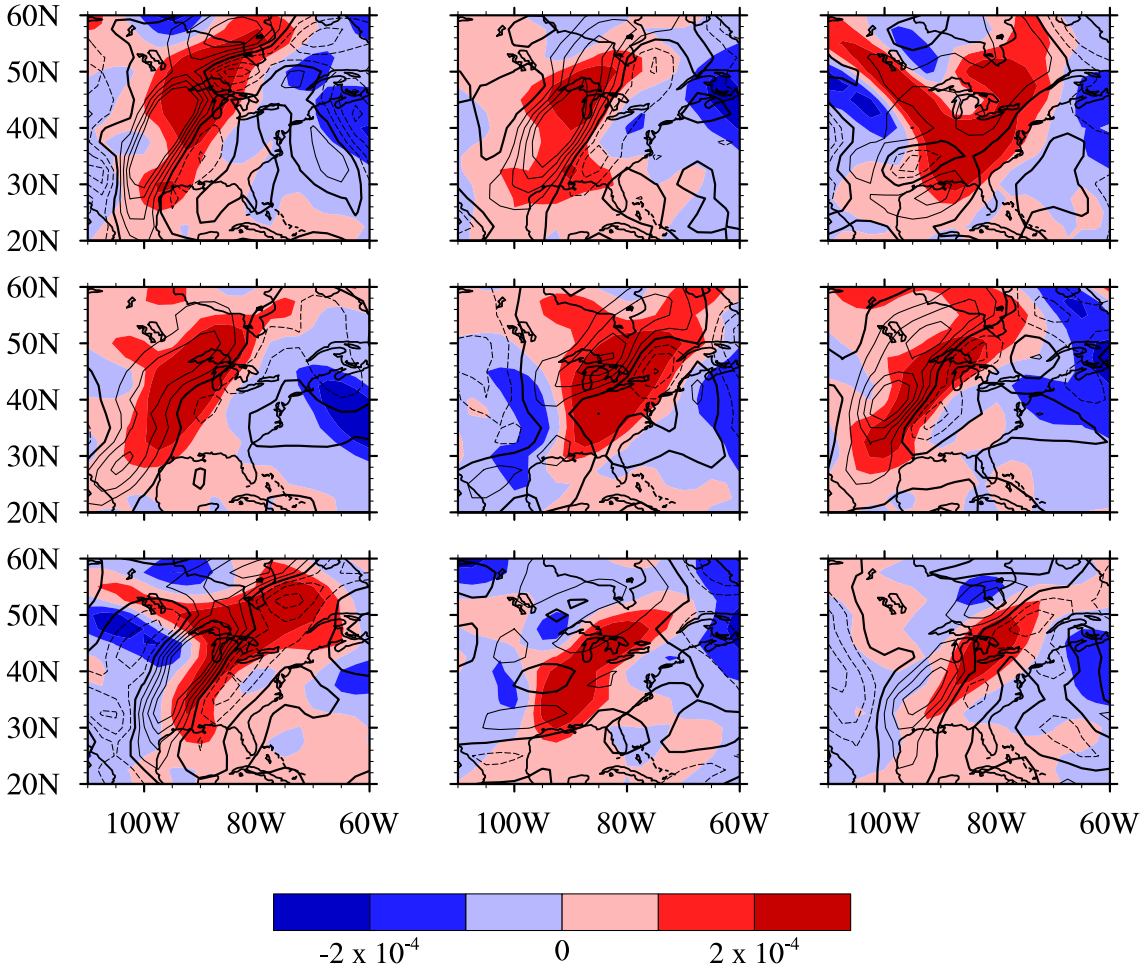

Fig. 23: *VA* (contours) and *TA* (shaded contours) on the days with the 9 highest combined $\tilde{C}$ and $q\mathbf{v}$ HEOF1 scores in DJF. Dashed contours indicate negative values, solid contours indicate positive values, and the zero *VA* contour is in bold. The contour interval for *VA* is 2×10^{-9} s^{-1}.

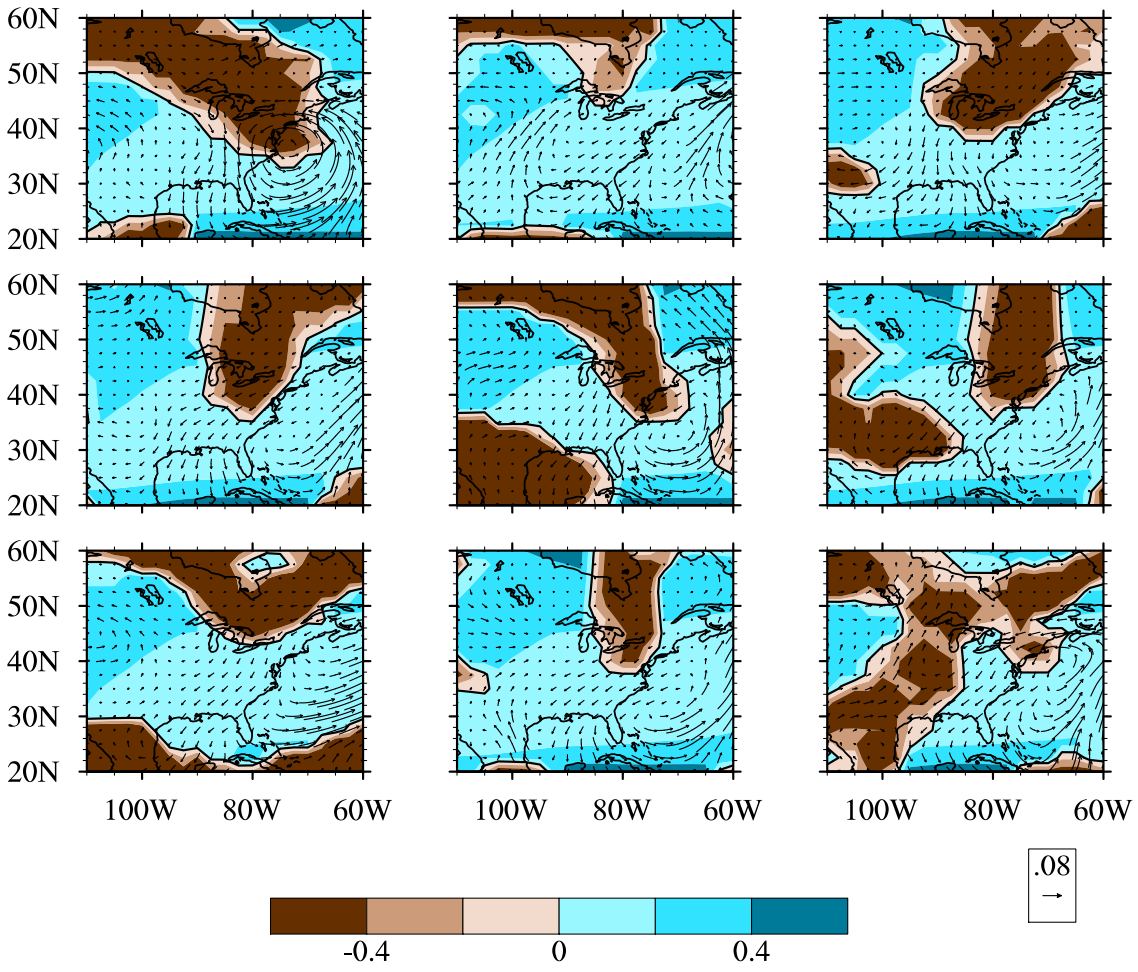

Fig. 24: $\tilde{C}$ (shaded contours) and $q\mathbf{v}$ (arrows) on the days with the 9 lowest combined $\tilde{C}$ and $q\mathbf{v}$ HEOF1 scores in DJF. The zero contour is in bold.

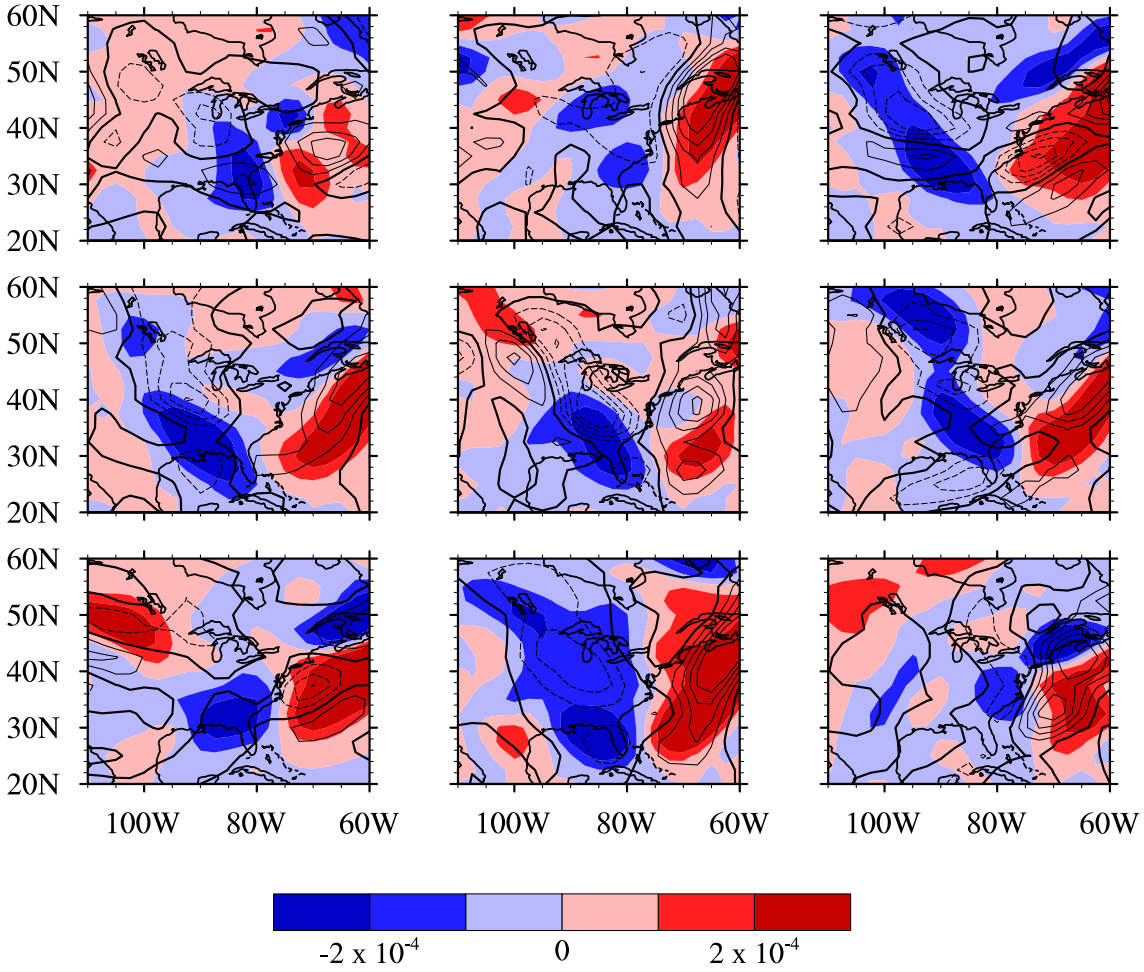

Fig. 25: *VA* (contours) and *TA* (shaded contours) on the days with the 9 lowest combined $\tilde{C}$ and $q\mathbf{v}$ HEOF1 scores in DJF. Dashed contours indicate negative values, solid contours indicate positive values, and the zero *VA* contour is in bold. The contour interval for *VA* is 2×10^{-9} s^{-1}.

precipitation (Fig. 17a), but are characterized by the absence of a strong upper-level jet, by weak *VA*, and by cold advection over Great Lakes, all of which are conducive to lake effect snow. However, in most cases the direction of 850-hPa moisture transport does not depict the north-northwesterly fetch that is associated with most lake effect snow events in the Great Lakes region. Thus, the low-score cases do not offer conclusive evidence of a lake effect snow environment.

Recall that the wave captured in the real part of HEOF1 of combined $\tilde{C}$ and $q\mathbf{v}$ is composed of two low-level circulations (Fig. 16). As noted in data and methods, the phase of the HEOF is arbitrary, and may be adjusted to optimize correlation with an external variable such as Midwest precipitation. However, the addition of π to the phase of HEOF1 of $\tilde{C}$ and $q\mathbf{v}$ in DJF depicted in Fig. 16a would reverse the moisture flow directions, resulting in the northerly component of 850-hPa flow necessary for lake effect snow. In the next section, an alternative phase shift for HEOF1 of combined $\tilde{C}$ and $q\mathbf{v}$ was calculated to highlight how lake effect snow relates to this propagating pattern.

3.4.1 Propagating patterns relevant to lake effect snow

A subset of stations was subjectively chosen to form a "lake effect" time series (P_l). The stations were located in Michigan near the eastern sides of Lake Michigan and the southern edge of Lake Huron downwind of the dominant northwest lake fetch (dark gray patches in Fig. 1). The fraction of total Midwest precipitation attributed to the lake effect stations was calculated as

$$P_l = \frac{\sum_{i=1}^{n} \beta\, p_i w_i}{\sum_{i=1}^{n} p_i w_i}, \tag{26}$$

where w refers to the area weights in data and methods, and n is the number of Midwest stations. The variable β is one if $i \in L$ and zero otherwise, where L is the set of lake effect stations (Fig. 1, dark gray shaded contours). Since lake effect snow tends to occur in conjunction with large-scale subsidence, the remainder of the Midwest domain is unlikely to experience precipitation during lake effect snow events, implying a relatively large P_l value. As done for total Midwest precipitation, a $1/4$ power transformation was applied to P_l, yielding the transformed time series $P_l^{0.25}$. P_l is undefined on days for which $P = 0$. The number of days with $P_l^{0.25} \geq 0.90$ is around 7 per season over the entire period, and is comparable to the climatology of days in DJF with snowfall > 1 inch $(2.54$ cm$)$ at two sites on the eastern side of Lake Michigan (Chagnon, 1968). Six winters of $P_l^{0.25}$ are shown in Fig. 26.

Composite anomalies for days with $P_l^{0.25} \geq 0.90$ (Fig. 27a) show north–northeasterly $q\mathbf{v}$ over the Midwest, including the Great Lakes region, implying weak moisture advection and a dominant northerly component of the 850-hPa wind field, consistent with cold advection over the lake surface as seen in Fig. 27b. As expected, the Midwest is in the exit sector of an upper-level trough (Fig. 27a), and is experiencing strong cold advection (Fig. 27b).

Phase-shifting the leading HEOF of combined $\tilde{C}$ and $q\mathbf{v}$ to maximize correlation between the real part of its score series and $P_l^{0.25}$ moves the pattern in Fig. 16a approximately one-half of a wavelength downstream, placing the Midwest in northeasterly $q\mathbf{v}$ and low $\tilde{C}$ (Fig. 28). However, the correlation of HEOF1 of combined $\tilde{C}$ and $q\mathbf{v}$ with DJF $P_l^{0.25}$ is only

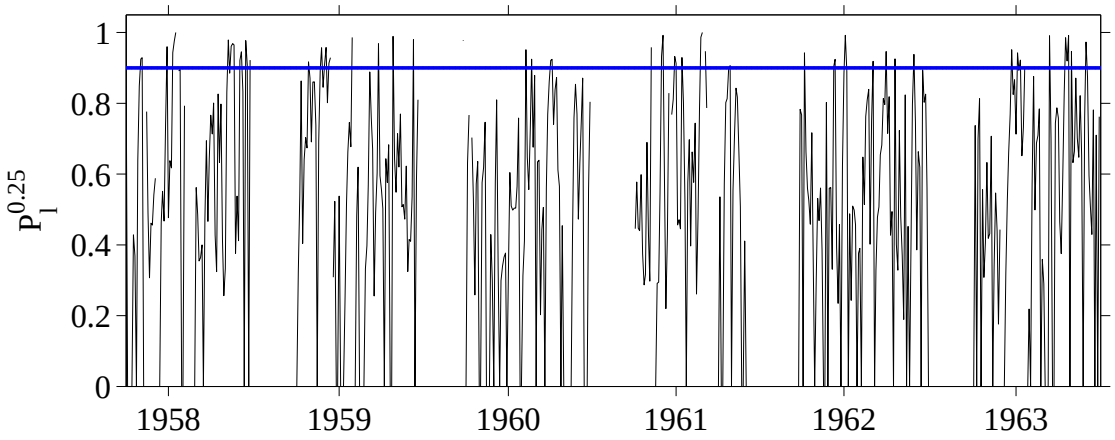

Fig. 26: $P_l^{0.25}$ for DJF 1957/1958–1962/1963. Tick marks are every Jan 1.

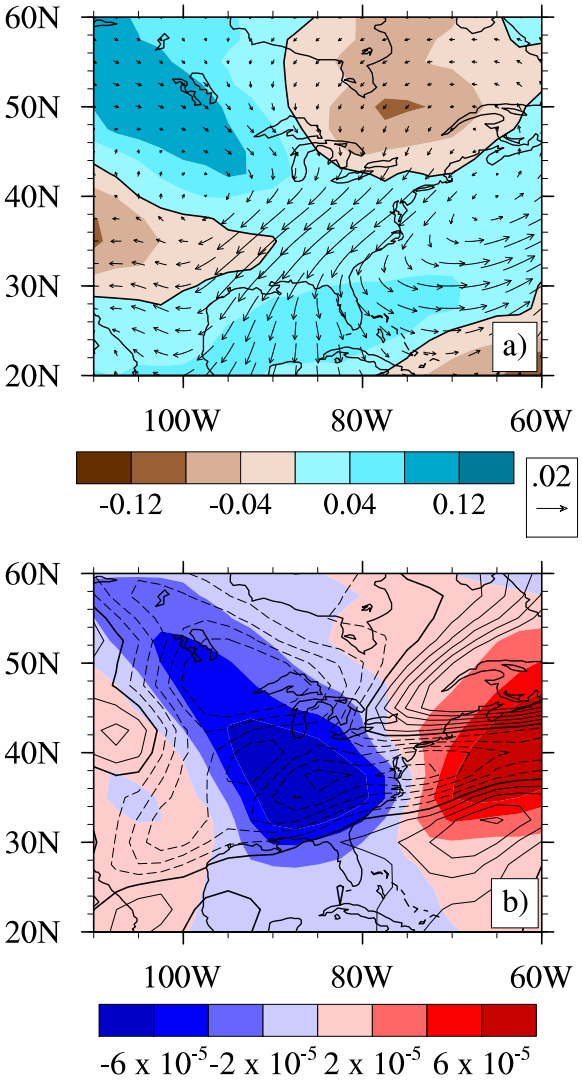

Fig. 27: Composite anomalies of a) $\tilde{C}$ (shaded contours) and $q\mathbf{v}$ (arrows) and b) *VA* (contours) and *TA* (shaded contours) for days with $P_l^{0.25} \geq 0.90$. The zero contours for $\tilde{C}$ and *VA* are in bold. The contour interval for *VA* is 1×10^{-10} s^{-1}.

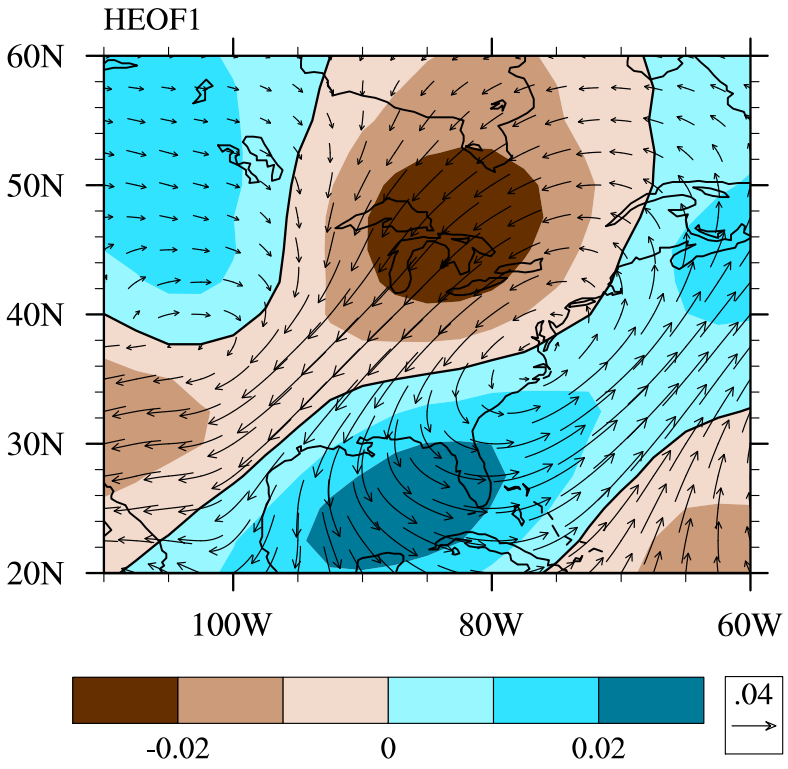

Fig. 28: HEOF1 of combined $\tilde{C}$ and $q\mathbf{v}$ phase-shifted to maximize the modulus correlation of the real part and $P_l^{0.25}$.

0.20 (significant at $\alpha = 0.05$). Though HEOF1 of combined $\tilde{C}$ and $q\mathbf{v}$ does not clearly resolve a lake effect pattern in the 850-hPa $q\mathbf{v}$ fields, the difference in ϕ_1 between the shifts corresponding to P_l and the Midwest precipitation timeseries is approximately π as anticipated.

Since the analysis domain is larger than the domain used to define lake effect precipitation stations, features outside of the Great Lakes region likely have the greatest impact on the direction of moisture transport. In fact, the magnitudes of the $q\mathbf{v}$ and $\tilde{C}$ loadings in Fig. 28 are relatively large over the Gulf of Mexico. Therefore, the phase shift that maximizes the correlation between the real part of HEOF of combined $\tilde{C}$ and $q\mathbf{v}$ and $P_l^{0.25}$ is probably weighted toward the large positive $\tilde{C}$ and, more importantly, the large negative $q\mathbf{v}$ values over the southern part of the domain. While reducing the latitudinal extent of domain of the HEOF analysis to 40°N–60°N produces a northwesterly fetch over the eastern Great Lakes region in HEOF1 of combined $\tilde{C}$ and $q\mathbf{v}$ (Fig. 29), it does not increase the correlation between $P_l^{0.25}$ and the real part of the score series. In addition, the cyclonic circulation is also located north and west of its position in Fig. 28, which suggests that the pattern is sensitive to the large decrease in the domain size.

3.5 Summer variability

Owing to the northward displacement of the jet stream and storm track, summertime precipitation in the central U.S. tends to result from isolated convective processes. In particular, mesoscale convective complexes (MCCs, Maddox, 1980) are responsible for a large portion of summer rainfall in the Midwest (Fritsch et al., 1986). MCCs generally contribute to the upper end of the precipitation distribution because of their relatively long duration and

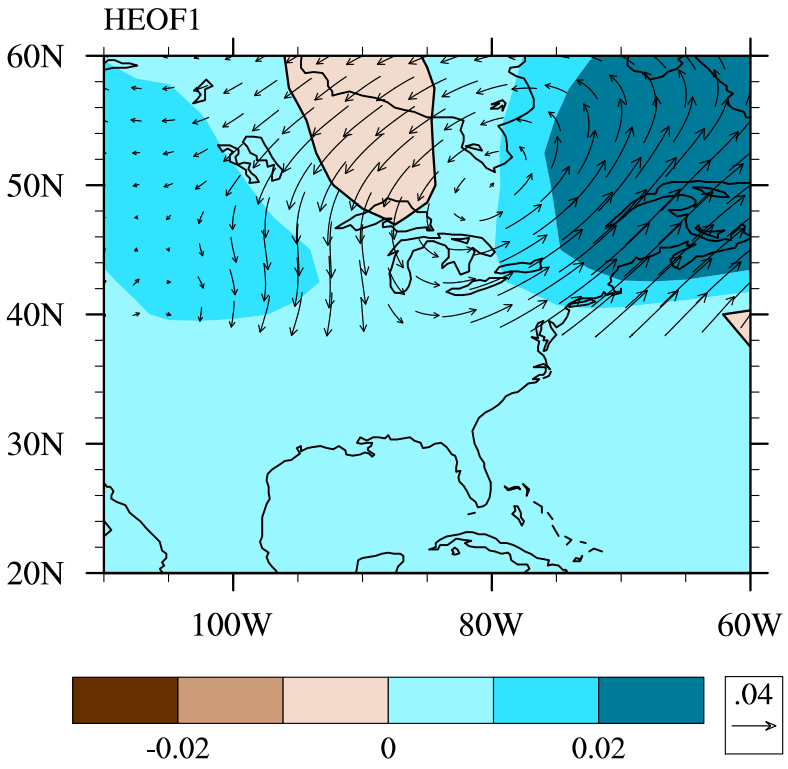

Fig. 29: HEOF1 of combined $\tilde{C}$ and $q\mathbf{v}$ phase-shifted to maximize the modulus correlation of the real part and $P_l^{0.25}$ with the domain bounded by 40°N-60°N.

high precipitation efficiency (Cotton et al., 1989). Furthermore, MCCs tend to form in moist environments with low vertical wind shear, often downstream of a weak midlevel trough, and are frequently preceded by a low-level jet (Maddox, 1983).

Anderson and Arritt (1998) noted similar conditions present during June and July 1993 – a period characterized by a large number of MCCs and persistent elongated convective systems (PECs), where PECs are differentiated from MCCs by their shape. A robust low-level jet and large-scale ascent were present in composites for both systems, though ascent was somewhat stronger for PECs than for MCCs. The area of negative 500-hPa height anomalies was also broader and centered farther east for PECs than for MCCs (their Fig. 8), suggesting that more intense upper level dynamics are involved in the production of PECs compared to MCCs. Results from Bell and Janowiak (1995) also revealed the presence of a 200-hPa jet streak within a ridge centered over the eastern U.S., and an upstream trough over the western U.S. during the 1993 Midwest floods. The right entrance region of the jet streak maintained an average position over the Midwest and Plains, resulting in persistent rising motion that likely assisted in the the development of the systems that generated much of the heavy precipitation.

The $q\mathbf{v}$ field in HEOF1 of combined $\tilde{C}$ and $q\mathbf{v}$ is a proxy for low-level moisture and the GPLLJ, both of which are key components in the production of warm season precipitation. Both the GPLLJ and MCCs tend to occur at night (e.g., Bonner, 1968; Maddox et al., 1982), meaning that a large portion of summer Midwest precipitation is likely nocturnal, as well. Using NNR data for MJJA 1985–1989, Higgins et al. (1997) showed that the presence of nocturnal (00–12 UTC) jets was associated with a greater percentage of precipitation over portions of the Midwest relative to the nocturnal mean, with the largest positive anomalies

tending to shift south and east throughout the season (their Figs. 12 and 13). This is consistent with shift in anomalies of vertically integrated moisture flux into the Midwest (their Fig. 20), which closely resemble HEOF1 of $q\mathbf{v}$ in May and June. During July and August, the cyclone-anticyclone couplet assumes a north–south position, and flow from the Gulf is maximized over the southeast U.S. and ORV.

By comparing the ratios of 90th percentile precipitation associated with strongest jets in July (P_{90}^{Upper}) to 90th percentile precipitation associated with the weakest jets (P_{90}^{Lower}), Monaghan et al. (2010) showed that the amount of nocturnal (0–4 LST) precipitation over the central U.S. is influenced by the intensity of the GPLLJ. $\frac{P_{90}^{\text{upper}}}{P_{90}^{\text{Lower}}}$ was impacted by the position of the jet exit region, as well, with the strongest jets exhibiting the greatest values of $\frac{P_{90}^{\text{upper}}}{P_{90}^{\text{Lower}}}$ for exit regions located north and northeast of the central Plains (their Fig. 6). These results are consistent with the findings in Tuttle and Davis (2006), which, in addition to linking jet strength to precipitation, identified the exit region of the GPLLJ as an area of convergence, instability, and potential frontogenesis.

Thus, one of the primary reasons for the weak relationship between HEOF1 of combined $\tilde{C}$ and $q\mathbf{v}$ and summer precipitation is its inability to resolve differences in the strength of the GPLLJ, which exhibits both diurnal and month-to-month variability, and is partly dependent on the strength of the upper-level jet. Because HEOF1 emphasizes the strongest features of the $q\mathbf{v}$ field, it is likely describing the GPLLJ in early summer, based on the month-to-month changes in the moisture flux field in Higgins et al. (1997). The positive $\tilde{C}$ anomalies present in the combined HEOF1 of combined $\tilde{C}$ and $q\mathbf{v}$ (Fig. 16) also indicates the propensity of HEOF1 of combined $\tilde{C}$ and $q\mathbf{v}$ to highlight a robust GPLLJ that occurs in conjunction with fairly strong synoptic forcing, as in the case of PECs in Anderson and Arritt (1998).

As a result, composites corresponding to the 9 highest and lowest combined $\tilde{C}$ and $q\mathbf{v}$ HEOF1 scores are highly variable. While $q\mathbf{v}$ anomalies are generally southerly (Fig. 30) and *TA* tends to be anomalously positive (Fig. 31) over most of the Midwest in the high-score cases, no primary pattern emerges in the low-score cases (Figs. 32 and 33). Furthermore, $\tilde{C}$ anomalies are overwhelmingly positive regardless of the score sign, while *VA* anomalies occur nearly equally in either case.

The strength of upper-level winds has been shown to influence the intensity of the GPLLJ as well. Composites of 200-hPa zonal wind and streamlines for strong GPLLJ events in Mo and Berbery (2004) (their Fig. 13) show a speed maximum (> 24 m s^{-1}) over the Great Lakes region embedded in a ridge with the entrance region aligned with the exit sector of the GPLLJ. Conversely, weak GPLLJ events are characterized by slower zonal winds, with a ridge over the central U.S. and a downstream trough centered over the Midwest. Similarly, Byerle and Paegle (2003) found that JJA vertically integrated moisture flux, 700- and 850-hPa wind, and precipitation over the central U.S., including parts of the Midwest, were positively correlated with 200-hPa zonal wind, particularly over the region encompassing the Rockies.

This is supported by Trenberth and Guillemot (1996), who found that Gulf moisture transport was a critical component of the large-scale circulation during the 1993 Midwest floods. However, it was the interaction of this moist flow with the southward shifted storm track, enhanced jet stream, and antecedent soil moisture that ultimately favored sustained heavy rainfall. Therefore, $q\mathbf{v}$, or any measure of atmospheric moisture for that matter, must be used in conjunction with other variables to definitively identify an environment conducive to heavy precipitation (i.e., horizontal moisture transport into the Midwest collocated with

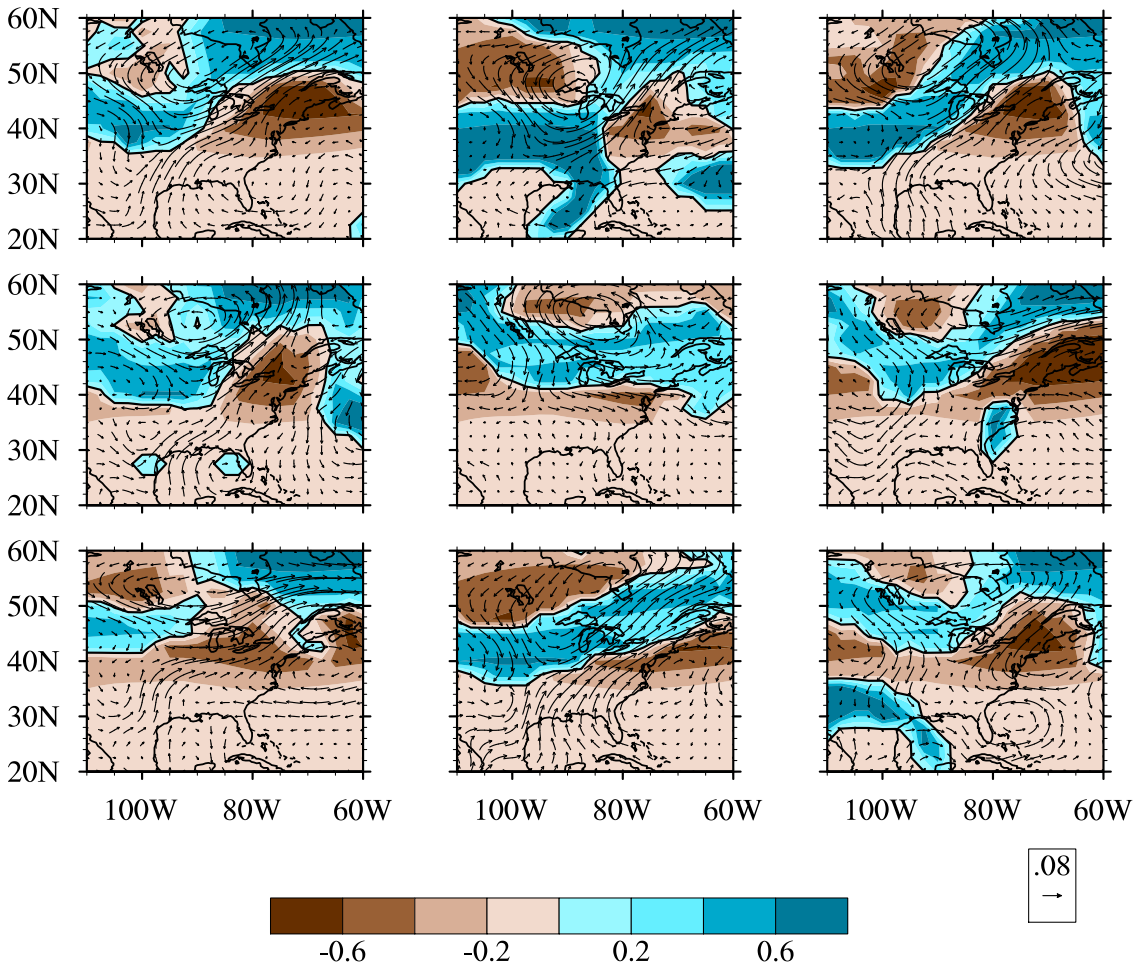

Fig. 30: $\tilde{C}$ (shaded contours) and $q\mathbf{v}$ (arrows) on the days the 9 highest combined $\tilde{C}$ and $q\mathbf{v}$ HEOF1 scores in JJA. The zero contour is in bold.

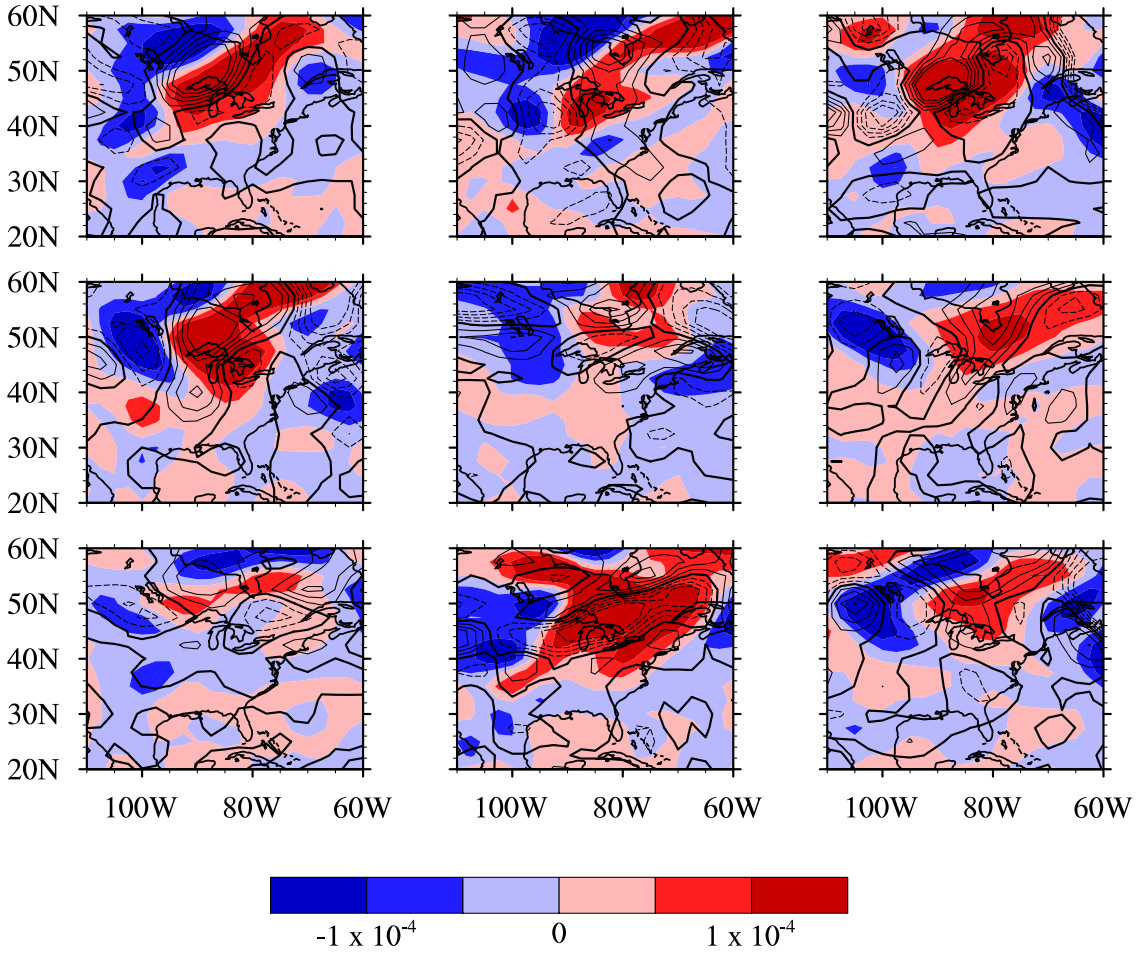

Fig. 31: *VA* (contours) and *TA* (shaded contours) on the days with the 9 highest combined $\tilde{C}$ and $q\mathbf{v}$ HEOF1 scores in JJA. Dashed contours indicate negative values, solid contours indicate positive values, and the zero *VA* contour is in bold. The contour interval for *VA* is $1 \times 10^{-9} \mathrm{s}^{-1}$.

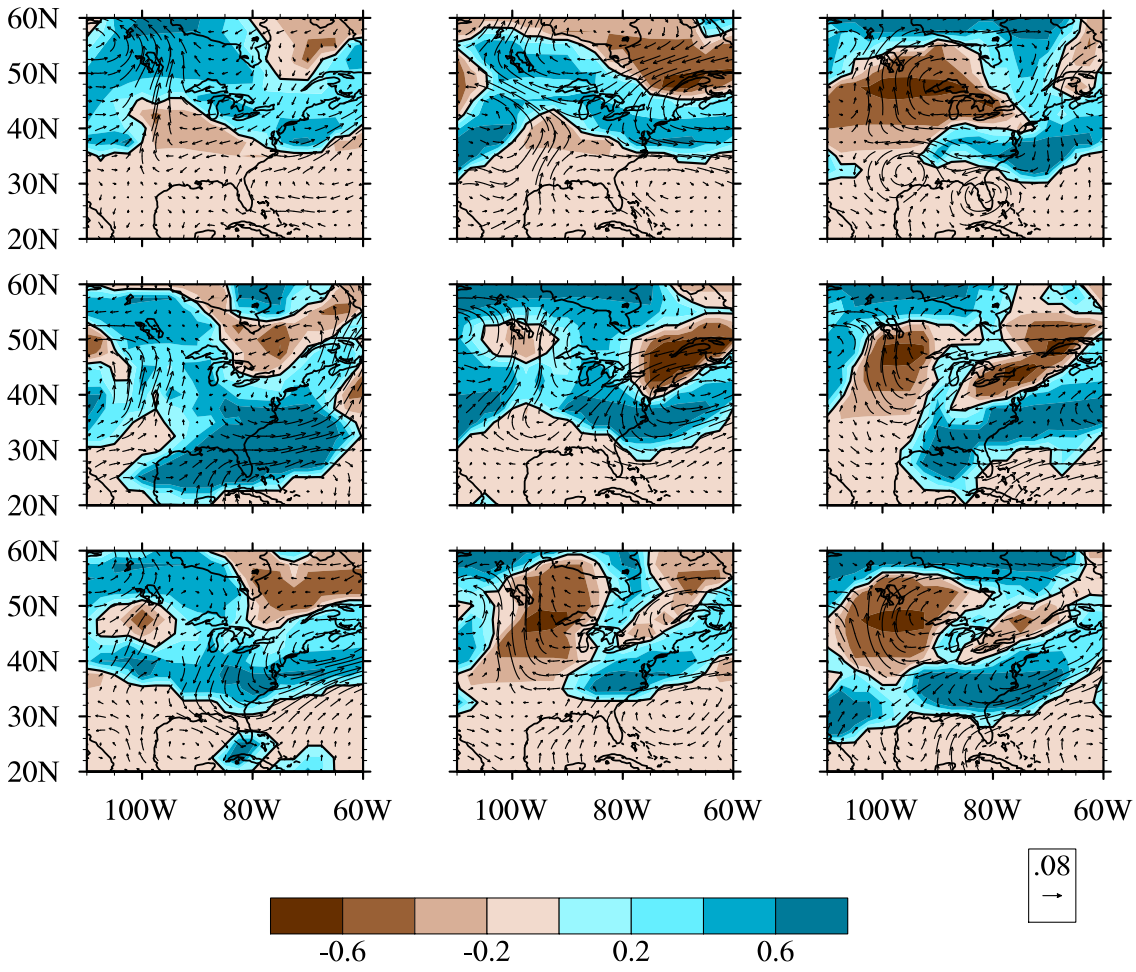

Fig. 32: $\tilde{C}$ (shaded contours) and $q\mathbf{v}$ (arrows) on the days with the 9 lowest $q\mathbf{v}$ HEOF1 scores in JJA. The zero contour is in bold.

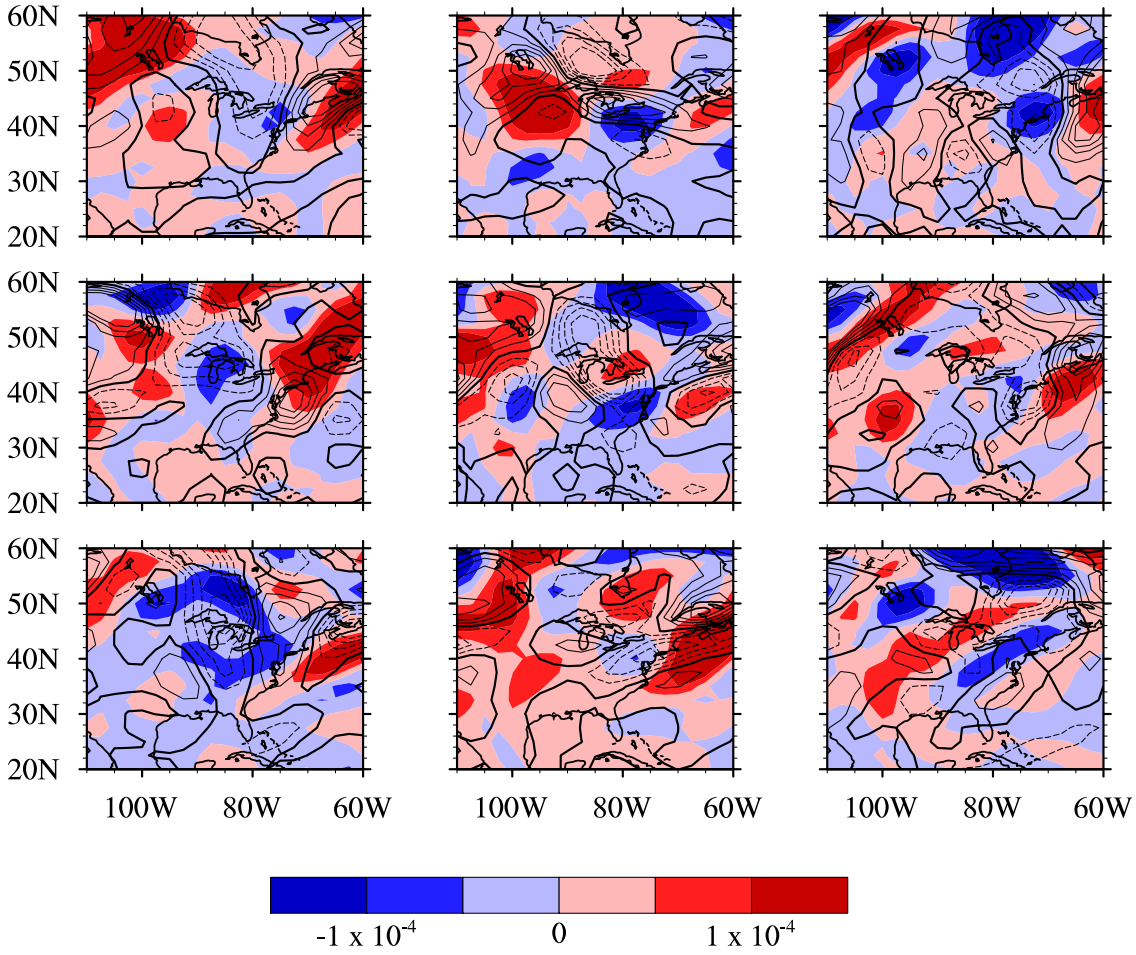

Fig. 33: *VA* (contours) and *TA* (shaded contours) on the days with the 9 lowest combined $\tilde{C}$ and $q\mathbf{v}$ HEOF1 scores in JJA. Dashed contours indicate negative values, solid contours indicate positive values, and the zero *VA* contour is in bold. The contour interval for *VA* is $1 \times 10^{-9} \mathrm{s}^{-1}$.

positive $\tilde{C}$ anomalies embedded in a ridge, and negative or weak positive *VA* anomalies). In all likelihood, JJA precipitation does not have one (or two) particular environments that typify heavy precipitation events. Thus, the leading HEOFs may primarily be capturing the characteristics of isolated events with large contributions to Midwest precipitation, such as the 1993 floods.

CHAPTER 4

SUMMARY AND CONCLUSIONS

Ultimately, the value of HEOF analysis lies in its ability to resolve propagating waves in a few simple patterns. Furthermore, relationships between a single HEOF and one or multiple time series are easily determined by adjusting the phase of the HEOF. While this particular analysis does not resolve any unexpected patterns of variability in Midwest regional circulation, it does condense most of the variability corresponding to daily precipitation into one HEOF, whereas traditional or rotated analysis would have produced two patterns approximately $\pi/2$ out of phase.

Both the composites and the leading HEOFs of $\tilde{C}$, *TA*, *VA*, and $q\mathbf{v}$ provide a reasonable representation of the environment conducive to precipitation in the Midwest. In addition, the pattern depicted in the composites of dry days, which is effectively opposite that of 90^{th} percentile precipitation days, is implicit in the negative loadings of these HEOFs. Furthermore, the fact that the HEOFs were computed independently of the precipitation time series, and the consistency in the patterns on different time scales, increases confidence that the composite anomalies are not merely byproducts of the statistical methods used.

Year-round analysis of 1958–2008 daily average $\tilde{C}$ and $q\mathbf{v}$ derived from the NNR data set over the Midwest produces the meridional migration of the jet and accompanying low-level circulation inherent in the annual cycle of both variables in HEOF1 of combined $\tilde{C}$ and $q\mathbf{v}$

("annual cycle" HEOF). The weighted precipitation time series is most highly correlated with HEOF2 of combined $\tilde{C}$ and $q\mathbf{v}$ ("storm HEOF") which depicts a jet stream oriented southwest-northeast over the central U.S., coupled with southerly 850-hPa flow into the domain. Together, the annual cycle and storm HEOFs account for two-thirds of the variance in the long-term weekly mean annual cycle of precipitation. Furthermore, the similarity between the storm HEOF and composite anomalies of $\tilde{C}$ and $q\mathbf{v}$ for 90^{th} percentile precipitation days indicates that the pattern is representative of actual atmospheric features associated with heavy precipitation.

The within-season analysis of the NNR-derived data revealed that HEOF1 of combined $\tilde{C}$ and $q\mathbf{v}$ has the strongest relationship with precipitation. The loadings show the same general wave feature present in the storm HEOF, which consists of a propagating cyclonic circulation over the central U.S. and a downstream anticyclonic circulation located along the East Coast, with moisture transport occurring from the Gulf of Mexico into the Midwest. The correlation between HEOF1 of combined $\tilde{C}$ and $q\mathbf{v}$ and precipitation is greatest in DJF and MAM, with the linear regression explaining approximately 45% of the variance in daily Midwest precipitation in both seasons.

Although HEOF1 of $q\mathbf{v}$ explains nearly the same amount of variance in $P^{0.25}$, HEOF1 of combined $\tilde{C}$ and $q\mathbf{v}$ provides the most comprehensive view of the regional propagating circulation features that influence precipitation because it indicates the position of the jet stream, the magnitude of moisture transport, the moisture source region, and the properties of the 850 hPa wind field. The latter is more informative because it provides additional information about jet-level variations. In addition, the $\tilde{C}$ pattern may be compared with teleconnection patterns in height or scalar wind fields.

In addition, applying a phase shift that maximizes the correlation between $P_l^{0.25}$ and the real part of HEOF1 of combined $\tilde{C}$ and $q\mathbf{v}$ in DJF shifts the pattern in HEOF1 of combined $\tilde{C}$ and $q\mathbf{v}$ approximately half of a wavelength downstream as expected in the case of a lake effect snow environment. However, the direction of moisture transport is not aligned with the fetch that is typical of most lake effect snow events in the Great Lakes region. The inability of HEOF1 of combined $\tilde{C}$ and $q\mathbf{v}$ to fully resolve the lake effect snow environment likely results from the large weighting of circulation features over the Gulf of Mexico, which has a larger influence on the correlation between the real part of shifted HEOF1 and $P_l^{0.25}$ than loadings over the Great Lakes region. Though adjusting the analysis domain of HEOF1 of combined $\tilde{C}$ and $q\mathbf{v}$ from 20°N–60°N to 40°N–60°N produces northwesterly $q\mathbf{v}$ over the eastern Great Lakes, the cyclonic circulation in the $q\mathbf{v}$ field is shifted north and west of its original position, indicating that the pattern is sensitive to large changes in the domain.

Overall, the HEOF analysis presented here isolated the components of the regional circulation that best explain Midwest precipitation resulting from propagating synoptic-scale features. This is evidenced by the strong relationship between HEOF1 of combined $\tilde{C}$ and $q\mathbf{v}$ and the PNA in DJF. As a result, HEOF1 of combined $\tilde{C}$ and $q\mathbf{v}$ has the strongest linear relationship with DJF precipitation, and is weakly correlated with precipitation in JJA when the jet stream shifts over the northernmost part of the domain and precipitation tends to result from convective processes. Though horizontal moisture transport is still the most important variable of the ones assessed in determining summertime precipitation, none of the HEOFs clearly capture mesoscale features, particularly MCCs, that are the main sources of precipitation during this time.

While combining $q\mathbf{V}$ with VA or $\tilde{C}$ results in a parsimonious representation of possible

sources of this instability, such as cyclonic *VA* or the dynamic processes associated with the jet stream, doing so produced HEOFs with more components than an analysis of a single variable. Thus, it is likely that multiple HEOFs of combined upper and lower-atmospheric features best approximate an MCC environment, with each one explaining a very small portion of the total field variance.

In addition, limitations arose from the fact the NNR data set is model-generated, meaning that it may smooth out mesoscale, or subtle large-scale, components of the flow that might otherwise indicate conditions favorable for convection. Also, the use of daily mean values of precipitation made it difficult to ascertain whether precipitation recorded on consecutive days resulted from a single event spanning multiple days, or separate daily events. This also produced uncertainty in determining the timing of precipitation with respect to the occurrence of atmospheric phenomena captured by the HEOFs.

Future work could, therefore, address these issues by using a different reanalysis with higher spatial and/or temporal resolution, such as the North American Regional Reanalysis (NARR), although the period of record only extends as far back as 1979. Another option is to compare HEOFs obtained from 6-hourly NNR data to a subdaily precipitation data set averaged over the same time period. Satellite or radar data could assist in the interpretation of the precipitation data, although these sources are not widely available prior to the 1970s, and often contain missing values. Whether different data are used or not, the methodology applied in this study is easily adaptable to other regions, provided the precipitation network over a given location is sufficiently dense.

REFERENCES

Agee, E. M., 1991: Trends in cyclone and anticyclone frequency and comparison with periods of warming and cooling over the Northern Hemisphere. *J. Climate*, **4**, 263–266.

Anderson, C. J., and R. W. Arritt, 1998: Mesoscale convective complexes and persistent elongated convective systems over the United States during 1992 and 1993. *Mon. Wea. Rev.*, **126**, 578–599.

Angel, J. R., and S. A. Isard, 1998: The frequency and intensity of Great Lakes cyclones. *J. Climate*, **11**, 1861–1871.

Ault, T. R., and S. S. George, 2010: The magnitude of decadal and multidecadal variability in North American precipitation. *J. Climate*, **23**, 842–850.

Aurenhammer, F., 1991: Voronoi diagrams–a survey of a fundamental geometric data structure. *ACM Computing Surveys*, **23**, 345–405.

Barlow, M., S. Nigam, and E. H. Berbery, 2001: ENSO, Pacific decadal variability, and US summertime precipitation, drought, and streamflow. *J. Climate*, **14**, 2105–2128.

Barnett, T. P., 1983: Interaction of the monsoon and pacific trade wind system at interannual time scales: Part I: The equatorial case. *Mon. Wea. Rev.*, **111**, 756–773.

Barnston, A., and R. E. Livezey, 1987: Classification, seasonality, and persistence of low-frequency atmospheric circulation patterns. *Mon. Wea. Rev.*, **115**, 1083–1126.

Bates, G. T., and M. P. Hoerling, 2001: Central U.S. springtime precipitation extremes: Teleconnections and relationships with sea surface temperature. *J. Climate*, **14**, 3751–3766.

Becker, E. J., and E. H. Berbery, 2009: Understanding the characteristics of daily precipitation over the United States using the North American Regional Reanalysis. *J. Climate*, **22**, 6268–6286.

Bell, G. D., and J. E. Janowiak, 1995: Atmospheric circulation associated with the Midwest floods of 1993. *Bull. Amer. Meteor. Soc.*, **76**, 6268–6286.

Bladé, I., 1999: The influence of midlatitude ocean-atmosphere coupling on the low-frequency variability of a gcm. Part II: interannual variability induced by tropical sst forcing. *J. Climate*, **12**, 21–45.

Bonner, W. D., 1968: Climatology of the low-level jet. *Mon. Wea. Rev.*, **96**, 833–850.

Bradbury, J. A., B. D. Keim, and C. P. Wake, 2003: The influence of regional storm tracking and teleconnections on winter precipitation in the Northeastern United States. *Ann. Assc. Amer. Geog.*, **93**, 544–556.

Byerle, L. A., and J. Paegle, 2003: Modulation of the Great Plains low-level jet and moisture transports by orography and large-scale circulations. *J. Geophys. Res*, **108**, doi: 10.1029/2002JD003005.

Chagnon, D., 1995: Determining cyclone frequencies using equal-area circles. *Mon. Wea. Rev.*, **123**, 2285–2294.

Chagnon, S. A., 1968: Precipitation climatology of Lake Michigan Basin. Bulletin 52, State Water Survey, 43 pp., Urbana, IL.

Coleman, J., and J. Rogers, 2003: Ohio River Valley winter moisture conditions associated with the Pacific–North American teleconnection pattern. *J. Climate*, **16**, 969–981.

Cotton, W. R., M. Lin, R. L. McAnelly, and C. J. Tremback, 1989: A composite model of mesoscale convective complexes. *Mon. Wea. Rev.*, **117**, 765–783.

Daly, C., W. P. Gibson, G. Taylor, M. Doggett, and J. I. Smith, 2007: Observer bias in daily precipitation measurements at United States cooperative network stations. *Bull. Amer. Meteor. Soc.*, **88**, 899–912.

DeGaetano, A. T., 2009: Time-dependent changes in extreme-precipitation return-period amounts in the continental United States. *J. Appl. Meteorol. Clim.*, **48**, 2086–2099.

E. W. Holroyd, I., 1971: Lake effect cloud bands as seen from weather satellites. *J. Atmos. Sci.*, **28**, 1165–1170.

Efron, B., 1981: Nonparametric standard errors and confidence intervals. Technical Report 67, Division of Biostatistics, Stanford University, 40 pp., Stanford, CA.

Eichler, T., and W. Higgins, 2006: Climatology and ENSO-related variability of North American extratropical cyclone activity. *J. Climate*, **19**, 2076–2093.

Fritsch, J. M., R. J. Kane, and C. R. Chelius, 1986: The contribution of mesoscale convective weather systems to warm season precipitation in the United States. *J. Climate*, **25**, 1333–1345.

Gershunov, A., and T. P. Barnett, 1998a: Enso influence on intraseasonal extreme rainfall and temperature frequencies in the contiguous united states: Observations and model results. *J. Climate*, **11**, 1575–1586.

Gershunov, A., and T. P. Barnett, 1998b: Interdecadal modulation of ENSO teleconnections. *Bull. Amer. Meteor. Soc.*, **79**, 2715–2725.

Groisman, P. Y., R. W. Knight, D. R. Easterling, T. R. Karl, G. C. Hegerl, and V. N. Razuvaev, 2005: Trends in intense precipitation in the climate record. *J. Climate*, **18**, 1326–1350.

Groisman, P. Y., R. W. Knight, T. R. Karl, D. R. Easterling, B. Sun, and J. H. Lawrimore, 2004: Contemporary changes in the hydrological cycle over the contiguous United States: trends derived from in situ observations. *J. Hydrometeorol.*, **5**, 64–85.

Hannachi, A., 2010: Toward a nonlinear identification of the atmospheric response to ENSO. *J. Climate*, **14**, 2138–2149.

Hannachi, A., I. T. Jolliffe, and D. B. Stephenson, 2007: Empirical orthogonal functions and related techniques in atmospheric science: A review. *Int. J. Climatol.*, **27**, doi: 10.1002/joc.1499.

Hartley, S., and M. J. Keables, 1998: Synoptic associations of winter climate and snowfall variability in New England, USA 1950–1992. *Int. J. Climatol.*, **18**, 281–298.

Hayden, B., 1999: Climate change and extratropical storminess in the United States:An assessment. *J. Amer. Wat. Resourc. Assoc.*, **35**, 1387–1397.

Higgins, R. W., V. B. S. Silva, W. Shi, and J. Larson, 2007: Relationships between climate variability and fluctuations in daily precipitation over the United States. *J. Climate*, **20**, 3561–3579.

Higgins, R. W., Y. Yao, E. S. Yarosh, J. E. Janowiak, and K. C. Mo, 1997: Influence of the Great Plains Low-Level Jet on summertime precipitation and moisture transport over the central United States. *J. Climate*, **10**, 481–507.

Hinkley, D., 1977: On quick choice of power transformation. *Appl. Stat.*, **26**, 67–69.

Holton, J. R., 2004: *An Introduction to Dynamic Meteorology*. 4th ed., Elsevier Academic Press, Burlington, MA.

Horel, J., 1981: A rotated principal component analysis of the interannual variability of the northern hemisphere 500 mb height field. *Mon. Wea. Rev.*, **109**, 2080–2092.

Horel, J., 1984: Complex prinicpal component analysis: Theory and examples. *J. Appl. Meteorol. Clim.*, **23**, 1660–1673.

Horowitz, J., 2001: The bootstrap. *Handbook of Econometrics*, J. J. Heckman and E. Leamer, Eds., Elsevier Science B.V., Vol. 5, 3160–3228.

Isard, S. A., J. R. Angel, and G. T. VanDyke, 2000: Zones of origin of Great Lakes cyclones in North America, 1899–1996. *Mon. Wea. Rev.*, **128**, 474–485.

Jolliffe, I. T., 2002: *Principal Component Analysis*. Springer-Verlag New York, Incorporated.

Kalnay, E. et al., 1996: The NCEP/NCAR 40-year reanalysis project. *Bull. Amer. Meteor. Soc.*, **77**, 437–470.

Karl, T. R., and R. W. Knight, 1998: Secular trends of precipitation amount, frequency, and intensity in the United States. *Bull. Amer. Meteor. Soc.*, **79**, 231–241.

Key, J. R., and A. C. K. Chan, 1999: Multidecadal global and regional trends in 1000 mb and 500 mb cyclone frequencies. *J. Geophys. Res*, **26**, 2053–2056.

Konrad, C. E., 2001: The most extreme precipitation events over the eastern United States from 1950 to 1996:Considerations of scale. *J. Hydrometeor.*, **2**, 309–325.

Kunkel, K. E., 2003: North American trends in extreme precipitation. *Nat. Hazards*, **29**, 291–305.

Kunkel, K. E., K. Andsager, and D. R. Easterling, 1999: Long-term trends in extreme precipitation events over the conterminous United States and Canada. *J. Climate*, **12**, 2515–2527.

Leathers, D. J., B. Yarnal, and M. A. Palecki, 1991: The Pacific/North American teleconnection pattern and United States climate. Part I: Regional temperature and precipitation associations. *J. Climate*, **4**, 517–528.

Lorenz, E. N., 1956: Empirical orthogonal functions and statistical weather prediction. Sci. Rep. No. **1**, Statistical Forecasting Project, Dept. Meteor., M.I.T., 49 pp.

Maddox, R. A., 1980: Mesoscale convective complexes. *Bull. Amer. Meteor. Soc.*, **61**, 1374–1387.

Maddox, R. A., 1983: Large-scale meteorological conditions associated with midlatitude, mesoscale convective complexes. *Mon. Wea. Rev.*, **111**, 1475–1493.

Maddox, R. A., D. M. Rogers, and K. W. Howard, 1982: Mesoscale convective complexes over the United States during 1981–Annual summary. *Mon. Wea. Rev.*, **110**, 1502–1514.

Mantua, N. J., S. R. Hare, Y. Zhang, J. M. Wallace, and R. Francis, 1997: A pacific interdecadal climate oscillation with impacts on salmon production. *Bull. Amer. Meteor. Soc.*, **78**, 1069–1079.

Mauget, S. A., 2003: Intra- to multidecadal climate variability over the continental United States: 193299. *J. Climate*, **16**, 2215–2231.

Mitchell, M. J., R. W. Arritt, and K. Labas, 1995: A climatology of the warm season great plains low-level jet using wind profiler observations. *Wea. Forecasting*, **10**, 576–591.

Mitchell, T. D., and P. D. Jones, 2005: An improved method of constructing a database of monthly climate observations and associated high-resolution grids. *Int. J. Climatol.*, **25**, 693–712.

Mo, K. C., and E. H. Berbery, 2004: Low-level jets and the summer precipitation regimes over North America. *J. Geophys. Res*, **109**, doi:10.1029/2003JD004106.

Mo, K. C., and J. E. Schemm, 2008: Droughts and persistent wet spells over the United States and Mexico. *J. Climate*, **21**, 980–994.

Monaghan, A. J., D. L. Rife, J. O. Pinto, and C. A. Davis, 2010: Global precipitation extremes associated with diurnally varying low-level jets. *J. Climate*, **23**, 5065–5084.

Namias, J., X. Yuan, and D. R. Cayan, 1988: Persistence of North Pacific sea surface temperature and atmospheric flow patterns. *J. Climate*, **1**, 682–703.

Newman, M., G. P. Compo, and M. A. Alexander, 2003: ENSO-forced variability of the Pacific Decadal Oscillation. *J. Climate*, **16**, 3853–3857.

Niziol, T. A., W. R. Snyder, and J. S. Waldstreicher, 1995: Winter weather forecasting throughout the Eastern United States. Part IV: lake effect snow. *Mon. Wea. Rev.*, **10**, 61–77.

North, G. R., T. L. Bell, R. F. Cahlan, and F. J. Moeng, 1982: Sampling errors in the estimation of empirical orthogonal functions. *Mon. Wea. Rev.*, **110**, 699–706.

Reitan, C., 1974: Frequencies of cyclones and cyclogenesis for North America, 1951–70. *Mon. Wea. Rev.*, **102**, 861–868.

Reitan, C., 1979: Trends in the frequencies of cyclone activity over North America. *Mon. Wea. Rev.*, **107**, 1684–1688.

Rodiionov, S. N., 1994: Association between winter precipitation and water-level fluctuations in the Great Lakes and atmospheric circulation patterns. *J. Climate*, **7**, 1693–1706.

Rothrock, H. J., 1969: An aid in forecasting significant lake snows. Tech Memo WBTM CR-30, National Weather Service, Central Region, 12 pp., Kansas City, MO.

R.R. Braham, J., 1983: The Midwest snowstorm of 8–11 December 1977. *Mon. Wea. Rev.*, **111**, 253–272.

Schneider, N., and B. D. Cornuelle, 2005: The forcing of the Pacific Decadal Oscillation. *J. Climate*, **18**, 4355–4373.

Serreze, M. C., M. P. Clark, and D. L. McGinnis, 1998: Characteristics of snowfall over the eastern half of the United States and relationships with principal modes of low-frequency atmospheric variability. *J. Climate*, **11**, 234–250.

Strong, C., and R. E. Davis, 2005: The surface of maximum wind as an alternative to the isobaric surface for wind climatology. *Geophys. Res. Lett.*, **32**, doi:10.1029/2004GL022039.

Strong, C., and R. E. Davis, 2008: Variability in the position and strength of winter jet stream cores related to Northern Hemisphere teleconnections. *J. Climate*, **21**, 584–592.

Trenberth, K., 1990: Recent observed interdecadal climate changes in the Northern Hemisphere. *Bull. Amer. Meteor. Soc.*, **71**, 988–993.

Trenberth, K., and C. J. Guillemot, 1996: Physical processes involved in the 1988 drought and 1993 floods in North America. *J. Climate*, **9**, 1288–1298.

Trenberth, K. E. et al., 2007: Climate Change 2007: The Physical Basis. Contribution of Working Group I to to the Fourth Assessment Report of the Intergovernmental Panel on Climate Change, chap. 3. Observations: surface and atmospheric climate change, 235–336. Cambridge University Press, Cambridge, UK.

Trigo, I. F., and T. D. Davies, 2000: Decline in Mediterranean rainfall caused by weakening of Mediterranean cyclones. *Geophys. Res. Lett.*, **27**, doi:10.1029/2000GL011526.

Tuttle, J. D., and C. A. Davis, 2006: Corridors of warm season precipitation in the central United States. *Mon. Wea. Rev.*, **134**, 2297–2317.

von Storch, H., T. Bruns, I. Fischer-Bruns, and K. Hasselmann, 1988: Principal oscillation pattern analysis of the 30- to 60-day oscillation in the general circulation model equatorial troposphere. *J. Geophys. Res*, **93**, 11 022–11 036.

Vose, R. S., R. L. Schmoyer, P. M. Steurer, T. C. Peterson, R. Heim, T. R. Karl, and J. K. Eischeid, 1992: The Global Historical Climatology Network:Long-term monthly temperature, precipitation, sea level pressure, and station pressure data. Technical Report ORNL/CDIAC-53, NDP-041, Carbon Dioxide Information Analysis Center, Oak Ridge National Laboratory, 325 pp., Oak Ridge, TN.

Wallace, J. M., and D. S. Gutzler, 1981: Teleconnections in the geopotential height field during the Northern Hemisphere winter. *Mon. Wea. Rev.*, **109**, 784–812.

Wernli, H., and C. Schwierz, 2006: Surface cyclones in the ERA-40 dataset (19582001). Part I: Novel identification method and global climatology. *J. Atmos. Sci.*, **63**, 2486–2507.

Wilks, D. S., 1995: *Statistical methods in the atmospheric sciences*. Academic Press, California.

Wolter, K., and M. S. Timlin, 1993: Monitoring ENSO in COADS with a seasonally adjusted principal component index. *Proc. of the 17th Climate Diagnostics Workshop*, Norman, OK.

Wolter, K., and M. S. Timlin, 1998: Measuring the strength of ENSO events: How does 1997/98 rank? *Weather*, **53**, 315–324.

Zhang, X., J. Wang, F. W. Zwiers, and P. Y. Groisman, 2010: The influence of large-scale climate variability on winter maximum daily precipitation over North America. *J. Climate*, **23**, 2902–2915.

Zishka, K. M., and P. J. Smith, 1980: The climatology of cyclones and anticyclones over North America and surrounding ocean environs for January and July, 1950–77. *Mon. Wea. Rev.*, **108**, 387–401.